Mid-to Late-Holocene Mediterranean climate variability: Contribution of multi-proxy and multi-sequence comparison using wavelet spectral analysis 2 in the northwestern Mediterranean basin

Julien Azuara, Pierre Sabatier, Vincent Lebreton, Bassem Jalali, Marie-Alexandrine Sicre, Laurent Dezileau, Maria Angela Bassetti, Jaime Frigola, Nathalie Coumbourieu-Nebou

Mid- to Late-Holocene Mediterranean climate variability: Contribution of multi-proxy and multi-sequence comparison using wavelet spectral analysis in the northwestern Mediterranean basin.

Azuara Julien[a*], Sabatier Pierre[b], Lebreton Vincent[a], Jalali Bassem[c], Sicre Marie Alexandrine[d], Dezileau Laurent[e], Bassetti Maria Angela[f], Frigola Jaime[g], Coumbourieu-Nebout Nathalie[a]

[a] HNHP, Muséum National d'Histoire Naturelle, UMR CNRS 7194, 75013 Paris, France

[b] EDYTEM, Univ. Grenoble Alpes, Univ. Savoie Mont Blanc, UMR CNRS 5204, 73000 Chambéry, France

[c] GEOGLOB, Université de Sfax, Faculté des Sciences de Sfax, 3038, Sfax, Tunisia

[d] LOCEAN, Sorbonne Universités (UPMC, Univ Paris 06), UMR CNRS-IRD-MNHN 7159, 75005 Paris, France.

[e] M2C, Université de Caen, UMR CNRS 6143, 14000 Caen, France

[f] CEFREM, Université de Perpignan, UMR CNRS 5110, 66000 Perpignan, France

[g] CRG Marine Geosciences, Department of Earth and Ocean Dynamics, Faculty of Earth Sciences, Universitat de Barcelona, 08028 Barcelona, Spain

*Julien.azuara@mnhn.fr

Keywords

Holocene ; Paleoclimatology ; Climate dynamics ; Mediterranean ;Wavelet spectral analysis ; Continental biomarkers ; Marine biomarkers ; Sediment mineralogy ; Vegetation dynamics

Abstract

Forcing and mechanisms underlying Holocene climate variability still remain poorly understood. This work review already published paleoclimatic time series and proposes an alternative way to compare them using spectral analysis. Such an approach may emphasize joint features between different signals and lead us closer to the causes of past climate changes.

Seven paleoclimatic proxy records from 2 sequences from the Gulf of Lion were compiled. These paleoclimate time-series were supplemented with proxies of the Atlantic area, the solar activity and a sequence recording El Niño–Southern Oscillations (ENSO) past variability. A comparison of their frequency content is proposed using wavelet spectral analysis for unevenly sampled time series. A new algorithm is used in order to propagate the age model errors within wavelet power spectra.

Two main groups of shared spectral features specific to the Mid- and Late Holocene (after 8200 yrs cal BP) can be defined on the basis of the results of these analyses, an Atlantic spectral feature (~1500 yrs) and two possible tropical Pacific spectral features (600-700 and 2000-2200 yrs). The Atlantic cyclic period is probably related to fluctuations of the Atlantic thermohaline circulation which would

induce changes in the storm track extension and position thereby impacting upon precipitation and storminess over a millennial scale. The ENSO variability spectral features which are registered in the Gulf of Lion proxies, potentially highlight a possible link between the tropical Pacific and the western Mediterranean climates during the Mid to late Holocene that needs to be further investigated.

Introduction

Until recently, the Holocene was often referred to as a stable climatic period. However, with the increasing resolution and diversity of paleoclimatic proxies, Holocene climate variability has progressively come to light. Interest in Holocene climate variability really started in the late 90s, when major features of this period became evident, such as the 8.2 kyrs event (Alley et al. 1997), Bond cycles (Bond et al. 1997, 2001) or the abrupt end of the African Humid Period (deMenocal et al. 2000). The development of this research field has followed increasing interest in current anthropogenic climate change. Indeed, disentangling changes induced by increased greenhouse gases in the atmosphere from the natural centennial scale climate variability is a crucial issue (Stocker et al. 2013).

Holocene rapid climate changes (RCCs) are now reported in many areas all over the world and by numerous types of proxies (Mayewski et al. 2004). Nevertheless, RCCs are not yet fully understood and the comparison of paleoclimatic proxies by simply comparing their curves can be confusing and frustrating when the number of time series increases. In this case, an alternative approach is to compare the time series in the frequency domain using spectral analysis in order to better understand the processes which generate their variability and possibly uncover underlying connections between them. However, spectral analyses classically apply to evenly sampled times series whereas paleoclimatic time series have an irregular temporal sampling. To overcome this issue, specific tools for spectral analysis of paleoclimatic time series have been developed in the past decades. Methods based on the Lomb-Scargle Fourier transform (Lomb 1976, Scargle 1982) for unevenly spaced data in combination with the Welch-Overlapped-Segment-Averaging algorithm (Welch 1967) were developed to deal specifically with paleoclimatic time-series avoiding the distortions associated with resampling at regular time steps (Schulz and Stattegger 1997, Schulz and Mudelsee 2002, Lenoir and Crucifix 2018a). Cross-spectral analyses relying on the same approach have also been developed to compare quantitively paleoclimatic time series in the frequency domain (Björg Ólafsdóttir et al. 2016). Paleoclimatic time series are also affected by uncertainties inherent to age-depth models and thus, algorithms have been developed to account for timescale errors due to age-depths models in such analyses, showing the influence of those errors on both spectral peak uncertainties and significance (Mudelsee et al. 2009, Rhines and Huybers 2011). Finally, the non-stationarity of the climate variability can be investigated by adapting wavelet spectral analysis to irregularly sampled time series allowing time/frequency analysis of paleoclimatic time series (Foster 1996, Lenoir and Crucifix 2018b, Polanco-Martinez and Faria 2018, Ghaderpour et al. 2018, Ghaderpour et al. 2019). Indeed, unlike the previous methods based on the Lomb-Scargle Fourrier transform, wavelet spectral analysis can be applied to non-stationary time series whose periodic features are not observed over their entire time range. Their application to paleoclimatic time series has highlighted the importance of non-stationarities to understand past climate variability (e.g. Witt and Schumann 2005, Polanco-Martinez and Faria 2018)

RCCs are detected by means of numerous proxies all over the Mediterranean basin: vegetation changes (e.g. Jalut et al. 2009, Combourieu-Nebout et al. 2009, Fletcher et al. 2013, Sadori et al. 2015, Jimenez-Moreno et al. 2015, Jaouadi et al. 2016), Sea Surface Temperature (SST) estimates (e.g. Sicre et al. 2016, Jalali et al. 2017), high molecular weight n-alkanes (e.g. Jalali et al. 2017), stable isotope analysis on speleothems (e.g. Bar-Matthews and Ayalon 2011, Smith et al. 2016), lake level fluctuations (e.g. Magny et al. 2002, 2003, 2007), flood frequencies (e.g. Wirth et al. 2013, Sabatier et al. 2017), thermohaline circulation proxies (e.g. Frigola et al. 2007, Siani et al. 2013), changes in windiness (e.g. Costas et al. 2016) or even storminess (e.g. Zazo et al. 2008, Billeaud et al. 2009, Sorrel et al. 2009, Dezileau et al. 2011, 2016, Sabatier et al. 2012, Raji et al 2015, Degeai et al. 2015, Orme et al. 2016), glacier advances (e.g. Giraudi 2005, Giraudi et al. 2011), African dust inputs (Bout-Roumazeille et al., 2013; Sabatier et al., 2020), etc. Nevertheless, while all of these proxies exhibit centennial scale climate variability, the timing of the RCC intervals often differs from one sequence to another. Taken together, these proxies reveal a very complex picture of Holocene climate variability within the Mediterranean Basin. Some authors stress the existence of contrasting geographical patterns, which structure climate variability and which can partly explain these discrepancies (Roberts et al. 2011, Magny et al. 2012, 2013, Peyron et al. 2013, Jalali et al. 2017). However, even within a restricted area, the correlation between RCCs is not always straightforward and age model uncertainties cannot account for all of the observed differences.

In order to better understand such complex patterns of climate variability in the Mediterranean region, we further develop a wavelet spectral analysis approach used by Witt and Schumann (2005) to deal with the non-stationarity of climate variability, and apply it to a set of climate proxies from a restricted area, the Gulf of Lion, to discuss past climate changes over a restricted time period, the Mid- and Late-Holocene from 8200 yrs cal BP to the present (Walker et al. 2012). We use an improved wavelet spectral analysis algorithm for irregularly sampled time series (Lenoir and Crucifix 2018b) and develop a new method to propagate age models' errors within wavelet spectral analysis, with a view to improving the reliability of wavelet spectra comparison. Additionally, the cross spectral analysis method proposed by Björg Ólafsdóttir et al. (2016) is used as a complementary tool to quantitatively compare the spectral content of the studied time series. The proxies used were produced within the framework of the MISTRALS/PaleoMeX research project. They are supplemented by published sequences from the near Atlantic area (northwestern Spain, inner Bay of Biscay) and time series recording possible drivers (solar variability) or major modes of climate variability (ENSO). Based on this dataset, our study aims to i) identify forcing influencing western Mediterranean climate variability over the past 8000 years, ii) investigate possible links between climate variability in this specific key region and the Atlantic or tropical areas, and iii) review elements of climatology that may explain the links we detect between the studied paleoclimatic time series.

Geographical and climatic context

The Gulf of Lion is a crescent-shaped continental margin located in the northwestern Mediterranean basin. It is surrounded by relatively narrow coastal plains and important mountain ranges within the hinterland of the eastern Pyrenees, the Massif Central and the Southern Alps (Figure 1). The coastal plains are bordered by numerous brackish lagoons that are the result of the interaction between a process of shore line regularization through the migration of sandy barriers, resulting from sediment transfer through littoral hydrodynamics, and the filling of these areas by fluvial and marine inputs (Raynal et al. 2009, Sabatier et al. 2010). The Massif Central and the Southern Alps are separated by the Rhône Valley. The Rhône, one of the major Mediterranean rivers, flows into the Mediterranean Sea in the eastern part of the Gulf of Lion, forming a wide delta and supplying large amounts of sediment (31 Mt yr^{-1}; Ludwig et al. 2009). Its wider drainage basin is influenced by both Mediterranean and temperate climates. The continental margin has a maximum width of 72 km with a water depth ranging between approximately 0 and 100m. Further offshore, the shelf slopes abruptly to the 2000 m deep abyssal plain (Bassetti et al. 2016).

This region is under the influence of a Mediterranean climate with cool mild winters and dry hot summers. In the lowlands, mean annual rainfall ranges from 500 to 800 mm (Rameau et al. 2008) with a maximum in autumn when cumulated October precipitations reach around 80mm, and a minimum in summer with cumulated July precipitations of less than 20mm (Météo France data, 1981-2010). Mean annual temperature is between 12 and 16°C (Rameau et al. 2008) with a maximum of around 23°C in July (monthly average) and a minimum of around 7°C in January (monthly average) (Météo France data, 1981-2010). However, the steep altitudinal gradient results in a decrease of seasonality with altitude. July precipitation increases with altitude while mean temperature decreases.

Large scale circulation patterns over the North Atlantic and Europe directly influence the western Mediterranean (Plaut and Simmonet 2001). Persistent high-pressure systems over the Arctic regions (Greenland, Iceland) and over Scandinavia tend to advect more Atlantic lows and rainfall toward the western Mediterranean. In contrast, when the Atlantic subtropical anticyclone (Azores high) shifts northwards, precipitation decreases. These large-scale circulation patterns also influence wind circulation. An anticyclonic blocking over the eastern Atlantic, associated with a low-pressure system over the central Mediterranean, induces cold, dry, northerly winds over the Gulf of Lion (Mistral and Tramontane, Figure 1) (Najac et al. 2009; Sicre et al. 2016), while persistent high-pressure systems over Scandinavia induce warm, humid, south-easterly winds (Plaut and Simonet 2001). Finally, large scale circulation patterns can contribute to the triggering of extreme climate events such as Heavy Precipitation Events (HPE; higher than 200mm in a day) (Joly et al. 2012, Nuissier et al. 2011) or summer heat waves (Cassou et al. 2005). Latitudinal shifts of the Atlantic zonal storm track associated with this general atmospheric circulation also influence the frequency and the intensity of northern Mediterranean storms cyclones (e.g. Trigo and DaCamara 2000, Nissen et al. 2010, Toreti et al. 2010) (Figure 1).

The complex orography of the northwestern Mediterranean basin and the interactions between the hinterland and the Mediterranean Sea promote mesoscale convective systems and greatly contribute to the regional climate specifics of this area. The Mediterranean Sea represents an important source of heat and moisture (Winschall et al. 2014). Warm and humid air advection from the Mediterranean towards the upland areas surrounding the Gulf of Lion causes significant rainfall and sometimes leads to HPE, such as that which occurred in the Gard on the 8-9 September 2002, when 600mm of rain fell in 24 hours (Nuissier et al 2011). The Gulf of Genoa is one of the major cyclogenesis regions of the whole Mediterranean basin and one of the most persistent throughout the year (Figure 1). The Gulf of Lion and the Balearic Islands, which are situated a few hundred kilometers to the west, are secondary centers of cyclogenesis linked to this very active and persistent center (Trigo et al. 1999, Lionello et al. 2016). Moreover, mesoscale cyclones formed in the Gulf of Genoa promote Mistral and Tramontane winds over the Gulf of Lion (Lebeaupin Brossier and Drobinski 2009).

Inter-annual climate variability in the western Mediterranean is greatly influenced by major patterns of atmospheric variability defined by differences in seasonal average sea-level pressures (SLP) at chosen locations. One of the most important is the North Atlantic Oscillation pattern (NAO) which involves inter-annual differences in the seasonal mean SLP between the Azores high and the Icelandic low (Hurrell et al. 2003). This pattern of variability is thus related to the strength of the meridional pressure gradient along the North Atlantic sector. A positive (negative) NAO index implies a higher (or lower) meridional pressure gradient which caused stronger (or weaker) westerlies. NAO variability has a considerable influence on the activity of the North Atlantic storm track during winter time (Rogers 1997, Hurrell et al. 2003). As a consequence, winter precipitation in the western-Mediterranean basin is higher and cyclogenesis is more pronounced during negative NAO years. The Mediterranean Oscillation pattern, involving contrasting pressure conditions between the western and the eastern Mediterranean, is a regional manifestation of the NAO (Conte et al. 1989). In addition, the Western Mediterranean Oscillation index (WeMOi), defined as the difference in pressure values between the Azores high and the Ligurian low systems, has been shown to detect variability in cyclogenesis in the western Mediterranean basin and thus is more effective that NAO for explaining seasonal precipitation in this area, especially on the east margin of the Iberian Peninsula (Martin-Vide and Lopez-Bustins 2006). The Scandinavian pattern (SCAND) is another important mode of inter-annual variability in the northern hemisphere, influencing the climate of the western Mediterranean region. It is defined as the SLP differences between Scandinavia and both Western Europe and Mongolia. Strong persistent positive pressure anomalies over Scandinavia cause enhanced precipitation in the central and western Mediterranean (Bueh and Nakamura 2007). Finally, the El

Niño Southern Oscillation (ENSO), which affects the tropical Pacific and Indian oceans, also impacts upon the European climate including that of the western Mediterranean area (Brönnimann et al. 2007). In winter, El Niño events can induce an atmospheric circulation pattern resembling a negative NAO, increasing winter precipitation rates in the western Mediterranean, but with sea level pressure anomalies shifted north-eastward. On the other hand, la Niña events can lead to a quasi-symmetric response, decreasing winter precipitation in the western Mediterranean (Brönnimann et al. 2007). In contrast, in Spring, El Niño events may induce a contrasting pattern characterized by dryer conditions in the western Mediterranean and wetter conditions in the area stretching from north-western Europe to the north western Iberian Peninsula; the opposite occurs during la Niña events. Nevertheless, it must be noted that these typical responses of European climate to ENSO are not always well recorded (Brönnimann et al. 2007). The ENSO signal in Europe is rather non-stationary and further work is needed to better characterize its modulating factors especially on decadal and multidecadal time-scales (Brönnimann et al. 2007).

Furthermore, the Gulf of Lion is one of the few areas where deep water formation occurs in the Mediterranean basin (MEDOC group 1970, Ulses et al. 2008, Frigola et al. 2007). Mediterranean waters are stratified in three different layers, i.e. surface, intermediate and deep waters. The surface waters (0-200m) originate in the Atlantic and flow eastwards through the Strait of Gibraltar becoming progressively warmer and saltier (Modified Atlantic Waters, MAW) (Figure 1). The intermediate waters (200-500m) form in the eastern Mediterranean during the winter season when dry, cold air from Anatolia causes surface waters to sink (Levantine Intermediate Waters, LIW) (Figure 1). Finally, the deep waters (>500m) form in the northern part of the Mediterranean basin where MAW is cooled by winds and mixed with LIW until they reach bottom water density and sink towards the abyssal plains (Western Mediterranean Deep Water, WMDW) (Rhein 1995, Schroeder et al. 2010). In the Gulf of Lion, the dry and cold Mistral and Tramontane winds are responsible for deep water formation (Figure 1). The Mistral blows from the north following the Rhône valley while the Tramontane blows from the northwest through the plain between the Pyrenees and the Massif Central. They both cause surface water heat loss within the gulf and thus lead to relatively low SST compared to the rest of the Mediterranean basin (Sicre et al. 2016). In summary, the climate of the Gulf of Lion results from the complex interactions between remotely driven processes and local features.

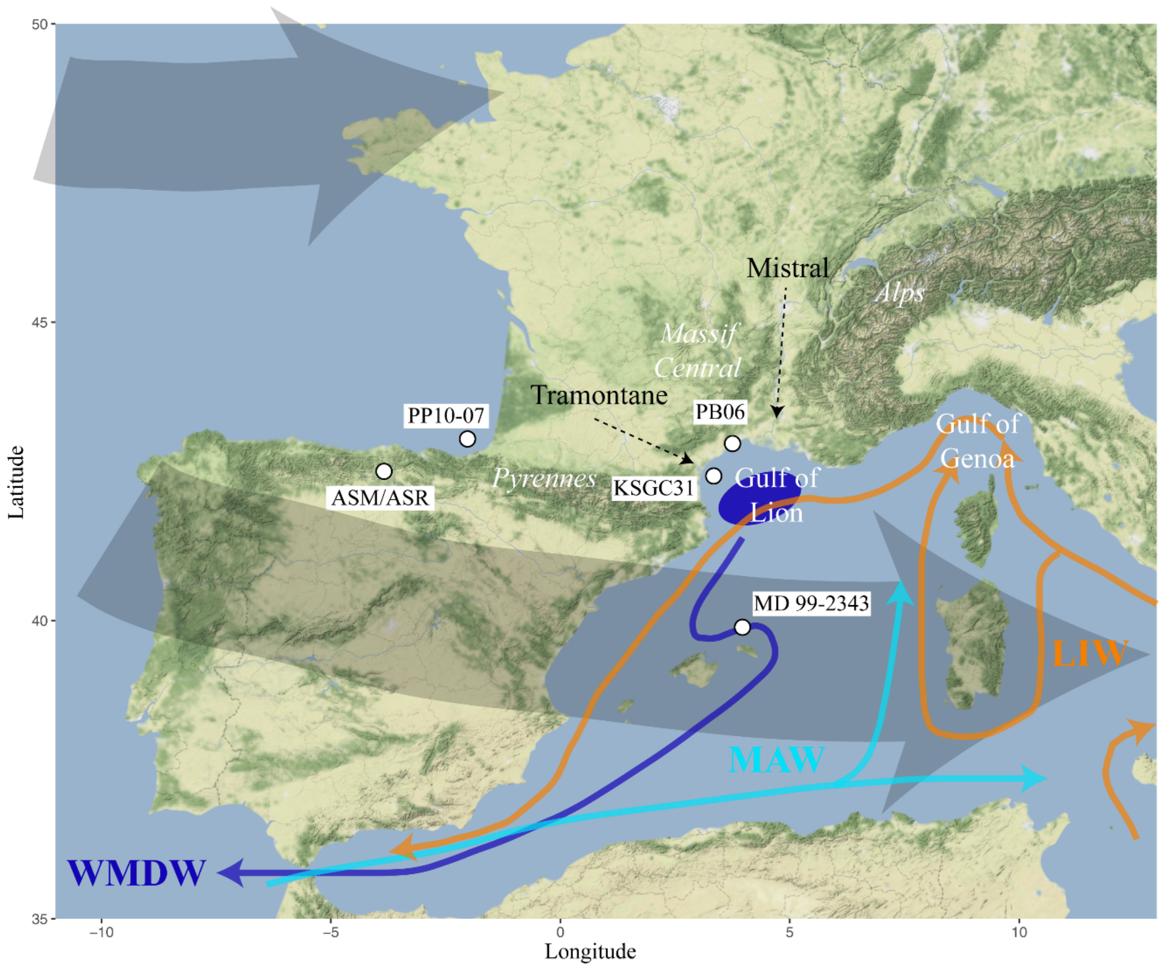

Figure 1: Locations of studied core sequences. Thin colored arrows represent marine currents (MAW, Modified Atlantic Waters; WMDW, Western Mediterranean Deep Waters; LIW, Levantine Intermediate Waters), black dotted arrows represent winds of southern France, and large shaded grey arrows represent the southern part of the Atlantic storm track. The blue oval represents the zone of formation of Western Mediterranean Deep Waters (WMDW).

Methods

The aim of this article is to compare paleoclimatic time series in the frequency domain in order to identify similar patterns of variability and to draw connections between distinct climate proxies. To this end, we used spectral analysis methods specifically adapted to deal with irregularly sampled time series, as the resampling with constant time-steps can introduce unpredictable biases in the results (Schulz and Stattegger 1997, Schulz and Mudelsee 2002, Witt and Schumann 2005, Pardo-Igúzquiza and Rodríguez-Tovar 2012, Polanco-Martínez and Faria 2018, Lenoir and Crucifix 2018a and b). Given the importance of non-stationarities to understand Holocene climate variability (Witt and Schumann 2005) we chose to analyze the data selected for this work using wavelet spectral analysis for unevenly sampled time series (Lenoir and Crucifix 2018b). Wavelet spectral analyses are designed to deal with non-stationary time series that allow us to determine the dominant modes of variability embedded in a signal and how these modes vary over time (Torrence and Compo 1998). On the other hand, the results of wavelet spectral analysis can display false dominant periodicities, especially for the lower frequencies that are of particular interest to us (Hochman et al. 2019). Thus, we chose to also use an univariate spectral analysis method for irregularly sampled time series developed by Schulz and Stattegger (1997) and Schulz and Mudelsee (2002) which, unlike wavelets, does not allow one to detect non-stationarities, but allows one to check whether the significant low frequency features detected in wavelet spectral analyses are actually present in the signal or not.

The central assumption of this work is that, if two signals share statistically significant features in the time/frequency space, they may be linked in some way; we review the mechanisms which could explain such a link. It is important to note that wavelet spectral analysis allows to characterize pseudo-periodic and non-periodic oscillations just as well as fully periodic oscillations. Here, we are looking for significant shared features in the wavelet spectra of the studied paleoclimatic time series; these features can highlight connections between spectra regardless of whether they are periodic or pseudo-periodic.

Wavelet spectral analysis, generalities

Wavelets are small wave functions with zero mean, localized in both the time and frequency domains. This means that they rapidly approach zero after few oscillations in the time domain and they display narrow-bandpass-like spectra in the frequency domain (admissibility conditions, Farge 1992, Torrence and Compo 1998). Wavelet function also need to have a number of oscillations that remain constant when they are translated or dilated, which makes it possible to generate from a single mother wavelet similar wavelet functions (daughter wavelets) that differ only in their localization in time and the frequency on which their Fourier transform is centered (similarity condition, Farge 1992). Therefore, a daughter wavelet is characterized by a non-dimensional time index (τ) quantifying its translation along the time axis and a scale (a) indicating the factor by which it has been dilated relatively to the mother wavelet.

The convolution of a time series with a daughter wavelet characterized by a given τ and a allows to investigate the contribution of a given frequency (related to the scale a by a formula depending on the mother wavelet) to the variability of the signal around the time τ; this is the continuous wavelet transform. By varying the scale and the time index, wavelet transforms allow to examine the contribution of a set of frequencies to the signal variability along the time series; this is why wavelet analyses are called “time/frequency analyses.” The results of such analyses are presented in the form of a scalogram, a graph with time in abscissa, scales or corresponding frequency or periods in ordinate, and the wavelet power (the square modulus of the wavelet transform) color coded. A periodic or pseudo-periodic feature of period λ that contributes to signal variability within the time interval $[t_1, t_2]$ is characterized by a power local maximum centered on λ between t_1 and t_2.

In this article, wavelets derived from the Morlet mother wavelet are used:

$$\psi_0(\eta) = \pi^{-1/4} e^{i\omega_0\eta} e^{-\eta^2/2}$$

The input η is a non-dimensional time parameter and ω_0 is the non-dimensional frequency, here equal to 5.5 in order to have the finest time resolution while satisfying the admissibility conditions (see Lenoir and Crucifix 2018b). The Morlet wavelet is a complex plane wave modulated by a gaussian. It is a nonorthogonal wavelet function better adapted to time series analysis than orthogonal wavelet functions because it is highly redundant at large scales so is more appropriate to catch smooth and continuous variations in wavelet amplitude. Moreover, as it is a complex function, the Morlet wavelet transform can be divided into a real and an imaginary part, which gives information about both amplitude and phase. The Morlet wavelet transform thus allows to better characterize oscillatory behavior in the analyzed time series than real wavelet functions, which are more useful for identifying isolated peaks and discontinuities. Finally, the Morlet wavelet is relatively wide compared to other complex nonorthogonal wavelets such as the Paul wavelet, which results in a lower resolution in terms of time but a better frequency resolution (Torrence and Compo 1998). Morlet wavelets are widely used for paleoclimatic time series analysis and more generally for geophysical and ecological data (i.e. Cazelles et al. 2008, Torrence and Webster 1999).

Wavelet spectral analysis of irregularly sampled time series

The scalogram under the formalism of orthogonal projection

In this study, wavelet spectral analyses are performed with the algorithm developed by Lenoir and Crucifix (2018b) which is a generalization of Foster's (1996) pioneering work, used by Witt and Schumann (2005) to analyze paleoclimatic time series in Greenland. However, it includes more sophisticated significance testing, scalogram smoothing and takes into account aliasing issues (Lenoir and crucifix 2018b). The main particularity of Foster (1996) and Lenoir and Crucifix (2018b) is to perform wavelet spectral analysis under the formalism of orthogonal projections. Unlike classical methods that define the continuous wavelet transform as the convolution product of a time series with a wavelet function, they define the continuous wavelet transform as an orthogonal projection on a vector space. In this approach, a time series X of length N is represented by two vectors of length N: the vector representing the measures $|X>$ and a vector representing the times $|t>$ at which the measures were made. The wavelet transform of X is the projection of the vector $|X>$ onto a vector space spanned by two linearly independent vectors (a plane), $G_{\tau,a}cos(|t>/a)$ and $G_{\tau,a}sin(|t>/a)$, which are the scaled sine and cosine of the time vector $|t>$ multiplied by a gaussian taper ($G_{\tau,a}$) varying with both time index and scale. The result of such a projection is a vector of length 2 whose components are its coordinates in the plane defined by the basis $\{G_{\tau,a}cos(|t>/a), G_{\tau,a}sin(|t>/a)\}$ and are analogous to the real and the imaginary part of the classical wavelet transform. The wavelet power plotted in the scalogram is simply the squared norm of this vector. Under this formalism, the wavelet transform gives very similar results to the classical approach and can easily be applied to irregularly sampled time series. Moreover, it is possible to define an orthogonal projection that is invariant with respect to the mean and the trend of a time series, allowing one to compute the wavelet transform and the scalogram without any preprocessing of the data.

The weighted smoothed scalogram

In spectral analysis, the data analyzed can be modeled by a periodic signal—a cosine or sine wave characterized by a frequency and an amplitude—with a long-term trend and noise superimposed on it. Under this assumption, a way to perform time/frequency analysis is to determine for a given time and a given frequency the amplitude characterizing this periodic component. If a frequency contributes strongly to the total variability of the signal at a given time, this will correspond to a strong amplitude for the periodic component, whereas if a frequency is absent, this will result in a zero amplitude. The result of such analysis is called the amplitude scalogram and is approximately proportional to the scalogram defined in the previous paragraph. It follows that, from a computational point of view, a convenient way to study how the amplitude of the periodic component varies in the time/frequency plane is to weight the scalogram by a factor related to the gaussian tapper $G_{\tau,a}$; this is the weighted scalogram.

Another issue is that the scalogram obtained from the analysis of a time series is not a consistent estimator of the true frequency content of the studied process. This means that the scalogram is just an estimation of the frequency content of the sampled signal varying with time, and, more importantly, that the error of this estimation does not converge to zero when the number of data points increase. From a practical point of view, this implies that the scalogram will remain noisy regardless of the quality of the data. In order to fix this problem, the scalogram needs to be smoothed. A weighted scalogram is smoothed over time by averaging the points of same scale (a) around a given time index (τ) within the time window $[\tau - \gamma\omega_0 a , \tau + \gamma\omega_0 a]$, with γ as the smoothing coefficient. Lenoir and Crucifix (2018b) recommend the use of the weighted smoothed scalogram in most time-frequency analyses of irregularly sampled time series; we thus use it in this article to analyze the studied paleoclimatic sequences.

Practical considerations

We used the WAVEPAL python package (https://github.com/guillaumelenoir/WAVEPAL), which allows time-frequency analysis of irregularly sampled time series using the weighted smoothed scalogram (Lenoir and Crucifix 2018b). The temporal resolution of the weighted smoothed scalogram, i.e. the number of time indices at which it is calculated, is equal to the length of the analyzed time series to avoid oversampling. For each time series, a polynomial trend is fitted by visual inspection. Even if the time series is not detrended, the degree of this polynomial trend is necessary to defined an orthogonal projection invariant with respect to this trend. The degrees of the polynomial trends fitted to the studied proxies are given in the Table 1. The smoothing coefficient $\gamma = 0.5$ was chosen for all sequences, and the length of integration was kept constant for a given scale when the smoothing interval intersected the edge of the time/frequency plane, meaning that parts of it were excluded from the analysis. One way to quantify the degree of smoothing is to use a scale independent index—in the case of smoothing over time (Maraun and Kurths 2004), the length of the time windows divided by the scale ($m = 2\gamma\omega_0$). Regarding this criterion, a smoothing coefficient of $\gamma = 0.5$ corresponds to a relatively high degree of smoothing ($m = 5.5$, Maraun and Kurths 2004). On the other hand, since the length of the smoothing time window depends on the scale, it implies that the smoothing will have little or no effect on smaller scales, since the smoothing time interval will contain only one or very few points to be averaged. Thus, for each of the time series, we give the period for which the smoothing interval contains at least 4 points (Table 1) and we call it the "minimum consistent period". For time series with large time steps (~50 yrs) one possibility would have been to increase the degree of smoothing by taking a higher smoothing coefficient; however such a choice would dramatically reduce the temporal resolution of the larger scales and for the present work, these larger scales are of more interest than small scales, considering the uncertainties of the age models of the studied time series (see below). Finally, for all time series, we used a coefficient of scale resolution equal to $\delta j = 0.05$, which is the largest value that gives an adequate sampling in scale for the Morlet wavelet (Torrence and Compo 1998). A smaller δj could have been used in order to have a finer resolution, but such a resolution would increase the time of the analysis, which can be a problem when quantifying the uncertainty due to age models (see below) without visibly improving the results.

Significance testing

The significance of the highlighted features in the time/frequency plane was statistically tested with hypothesis testing using the WAVEPAL and CARMA (https://github.com/brandonckelly/carma_pack) python packages. For each point of the time/frequency plane, we independently tested the null-hypothesis (H_0) that there is no periodic component in the analyzed signal for a given scale (i.e. frequency) and time index pair. To this end, the distribution of each point of the weighted smoothed scalogram was calculated under the null-hypothesis and the points of the data scalogram above the X^{th} percentile were considered to be significant with a (100-X)% level of significance, entailing a rejection of the null-hypothesis with X% confidence (Lenoir and Crucifix 2018b). For all analyses, the 5 and 10% confidence levels were plotted on the scalograms.

A crucial step for this significance testing is to correctly estimate the distribution of points on the scalogram under the null hypothesis, derived analytically (Lenoir and Crucifix 1998). Under the null hypothesis, the analyzed time series is considered to be a trend with background noise superimposed on it, so the characteristics of this noise are crucial to derive reliable distributions. In Lenoir and Crucifix (2018), the background noise is modeled by a zero-mean stationary Gaussian CARMA (Continuous Autoregressive Moving Average) process, sampled at the times $|t >$ of the time series. CARMA processes are a way to model stochastic processes in continuous time in order to have a better representation of underlying physical processes which are actually continuous. This allows to work easily with irregularly sampled time series (Kelly et al. 2009, 2014) compared to discrete autoregressive process commonly used when working with regularly sampled data (Torrence and Compo 1998). CARMA (p, q) processes are characterized by their order p and q, which represent the number of terms in the left and right part of the model's stochastic differential equation. In practice, only CARMA processes of low order are useful in the context of spectral analysis since high order CARMA processes can display dominant spectral peaks even when they are purely random. A CARMA $(0,0)$ process is equivalent to white noise, i.e. a random process normally distributed. A CARMA $(1,0)$ process is equivalent to a continuous first-order autoregressive process (also called a Ornstein-Uhlenbeck process) which is the continuous-time analog (Kelly et al. 2009, 2014) of the widely used first-order autoregressive process (AR1) for significance testing in spectral analysis (e.g. Torrence and Compo 1998, Schulz and Mudelsee 2002).

In this article we choose to use a CARMA (1,0) process as background noise for the significance testing. Indeed, spectra of paleoclimatic time series often display a decreasing spectral amplitude with increasing frequency, which can be explained simply by a random AR(1) process (Hasselmann 1976, Schulz and Mudelsee 2002). Assuming that the studied time series is a just trend with a CARMA(1,0) process superimposed on it (null-hypothesis), the trend is removed and the CARMA python package is used to estimates the characteristics of this noise. The WAVEPAL package is then able to analytically compute the distribution of the scalogram points and the corresponding confidence level from the previous results.

Edge effects and aliasing issues

In classical wavelet spectral analysis of regular sampled time series using the convolution function method, errors are likely to appear at the margins of the scalogram because the time series analyzed are of finite length and the use of the Fourrier transform assumes the data is cyclic (Torrence and Compo 1998, Zhang and Moore 2011). One way to solve this problem is to pad the end of the time series with zeros before performing the wavelet transform; however, this zero-padding will decrease the amplitude of the result near the edge of the time/frequency plane. This is why a "cone of influence" is usually plotted on a scalogram to visualize where such edge effects become important and cannot be neglected (Torrence and Compo 1998, Zhang and Moore 2011). Under the formalism of orthogonal projections, Fourier transforms are not used so there is no need for zero-padding, but this doesn't mean that there are no edge effects in the scalogram. Indeed, near the edge of the time series, in areas in which length increases with the scale, part of the wavelet supports can stand outside bounds of the data (Lenoir and Crucifix 2018b). This implies that, in these parts of time/frequency plane, the small waves of the $G_{\tau,a}cos(|t>/a)$ and $G_{\tau,a}sin(|t>/a)$ vectors on which the data vector $|X>$ is projected are truncated at one end as they approach zero, which can of course affect the results of the analysis. For this reason, a "cone of influence" is also defined under the formalism of orthogonal projection for those regions where edge effects are not negligible (Lenoir and Crucifix 2018b). The length of this "cone of influence" on each side of the time/frequency plane is proportional to the width of the wavelet and is given by the formula $\sqrt{2}\omega_0 a$ (Torrence and Compo 1998, Lenoir and Crucifix 2018b). The "cone of influence" corresponds to the shaded grey area on both sides of the scalograms.

In the case of irregularly sampled time-series, the scale of the wavelet packet may be too low compared to the local time step, leading to the erroneous detection of high frequency periodicities which are not present in the signal. This bias, called aliasing, can be prevented by excluding from analysis some areas of the time-scale plane (Lenoir and Crucifix 2018b). These excluded areas form the Shannon-Nyquist exclusion zone (SNEZ), with reference to the Shannon-Nyquist sampling theorem from which they are calculated. The SNEZ is represented in black at the bottom of the scalograms. Due to correlation between neighboring scales and to smoothing in the scalogram, the SNEZ must be slightly extended (Lenoir and Crucifix 2018b). In the scalograms, this extension of the SNEZ is the shaded grey area just above the SNEZ.

Finally, according to a recommendation in Lenoir and Crucifix (2018b), we chose a fixed length of integration when computing the weighted smoothed scalogram. This resulted in two more excluded areas in black at the right and the left of the scalogram.

Propagation of age model uncertainties in wavelet spectral analysis

Most paleoclimatic sequence chronologies are based on radionuclide measurements and are therefore affected by age model uncertainties. These uncertainties introduce an inherent bias within all types of spectral analysis (Mudelsee et al. 2009, Rhines and Huybers 2011). In most of the papers dealing with spectral analysis of paleoclimatic sequences this problem is not considered and not even mentioned, despite the fact that it can affect both the significance of a spectral peak and the estimation of its position (Mudelsee et al. 2009). Even if there is no way to avoid this bias, it is possible to quantify it. For this study, a short program based on a Monte Carlo method was written with Python to propagate age model errors within wavelet spectral analysis and to estimate their effect on the position of the scalogram maxima along the scale (period) axis. Such a method for propagating age model uncertainties has been used previously by Anchukaitis and Tierney (2013) to conduct an empirical orthogonal function analysis on proxies from different sequences.

First, the age models of all the studied time series were recalculated from scratch with the RBACON R package for age-depth modeling using Bayesian statistics (Blaauw and Christen 2011, https://CRAN.R-project.org/package=rbacon). At the same time, 3000 alternative age models without age reversals were generated with RBACON for each time series using the same method. The most straightforward way to address the issue of age model error would have been to use these alternative age models to compute 3000 alternative weighted smoothed scalograms for each time series. This would have allowed an easy evaluation of the impact of the age model uncertainties on each point of the time/frequency plane. However, this is not practical due to the computation time required to calculate a single weighted smoothed scalogram (several minutes for most of the time series studied here), resulting in an algorithm requiring several days to perform a single analysis. Thus, we decided to characterize the significant features of our scalograms by looking at the position of local maxima in scalogram “slices” along the period axis and propagate the age model uncertainties only for these selected slices. The positions of local maxima observed in a scalogram may of course vary with the time indices of the chosen slices; nevertheless, maxima positions will vary very gradually as the adjacent points of a scalogram are highly correlated along the time axis (Maraun and Kurth 2004).

Let’s take an example to see how the algorithm works. Let’s consider a time series call X with $|X >$ the vector of its measures and $|t >$ the vector of its sampling times. A simple visual observation reveals that the weighted smoothed scalogram of X displays a significant local maximum between $[t_1, t_2]$ at a period around λ_{obs} (The WAVEPAL python package allows horizontal dashed lines to be drawn across the scalogram, which is convenient for approximating periods). In order to evaluate the consequences of age model errors on the period characterizing this maximum we use the following procedure:

- A time t_{obs}, with $t_1 < t_{obs} < t_2$, is chosen by visual observation where the local maximum around λ_{obs} is particularly well marked
- The program will calculate the exact period λ_{calc} of this local maximum for the time index $t_{calc} \in |t >$ closest to t_{obs}.
- Then 3000 scalogram slices for this time index t_{calc} will be calculated with exactly the same parameters but 3000 different time vectors $|t >$.
- The program will then search in each of these 3000 scalogram slices for the alternative local maximum $\lambda_{alt,i}$ closest to the reference value λ_{calc} to obtain 3000 possible period values.
- Finally, 5th and 95th quantiles of the 3000 $\lambda_{alt,i}$ distribution will be used to define an interval within which the true period will theoretically have a 90% chance of being found.

This method allows us to address the influence of age model uncertainties on period estimates in a rapid and straightforward way. On the other hand, for computational practicality, we were obliged to compute the 3000 alternative scalogram slices without smoothing. As mentioned above, the unsmoothed scalogram is not a consistent estimator of the frequency content; nevertheless, this does not appear to be a major problem in this particular case. Before each analysis, we compared, for the chosen time index, the period of the local maximum obtained with the smoothed and unsmoothed weighted scalograms in order to assess the discrepancy between the two. In most cases the values found were strictly identical, and when they were not, they remained extremely close (Appendix 1, Table I). As already mentioned, adjacent points of the raw scalogram are highly correlated along the time axis (Maraun and Kurths 2004) and the smoothing performed mostly affects the absolute value of the local maxima in the scalogram and not their position along the period axis.

Welch's Overlapped Segment Averaging method

The REDFIT program (Schulz and Mudelsee 2002) was used to re-analyze all the paleoclimatic time series using an independent method of spectral analysis in order to check the reliability of low frequency features detected with wavelet spectral analyses. The algorithm of the REDFIT program is based on the Lomb-Scargle Fourier transform (Lomb 1976, Scargle 1982) and Welch's Overlapped Segment Averaging procedure (Welch 1967, WOSA method). Just as for the raw wavelet scalogram, the raw auto-spectrum of a time series obtained from the Lomb-Scargle Fourier transform is not a consistent estimator of its true frequency content—it needs to be smoothed. Thus, the time series is divided into several segments with 50% overlap. A linear trend is subtracted from each segment to avoid biases at low frequencies. Then, each segment is multiplied by a chosen taper to reduce spectral leakage. Finally, the auto-spectrum (periodogram) of the time series is calculated as the average of the Lomb-Scargle Fourier transforms of all the detrended and tapered segments (Schulz and Stattegger 1997, Schulz and Mudelsee 2002).

In practice, we used the Welch taper for most of our analyses (Welch 1967). Tests realized using other available tapers in the REDFIT program gave us equivalent results. On the other hand, the number of segments is a key parameter of this method. For a time series with a given number of points, a larger number of segments will reduce the noise in the auto-spectrum but also decrease the frequency resolution, reducing at the same time the minimum frequency (i.e. the maximum period) that can be investigated. Since we are particularly interested in low frequencies (long periods), we used relatively small numbers of segments (between 3 and 5) which in each case allowed us to obtain information on periods up to 2000 years while maintaining a satisfactory degree of smoothing. These numbers of segments are consistent with those found in the bibliography for time series with numbers of points of the same order of magnitude as those studied here (e.g. Oppenheim et al. 1999, Schulz and Mudelsee 2002). The results of these analyses are referred to in the Discussion, and are presented in detail in Appendix 1.

Comparison of time series in the frequency domain

To compare time series in the frequency domain, methods of cross-spectral analysis with statistical tests of significance must be used. Wavelet coherency analysis would have been ideal (Maraun and Kurths 2004), but this method is not implemented in the WAVEPAL python package and, to best of our knowledge, has not yet been adapted for irregularly sampled time series. We thus decided to use the program REDFIT-X for cross-spectral analysis of unevenly spaced paleoclimate time series (Björg Ólafsdóttir et al. 2016) which generates a coherency spectrum based on the WOSA method (see paragraph above).

The coherency of two time series x and y is defined as the squared modulus of their cross-spectrum (G_{xy}) normalized by the product of their auto-spectrum (G_{xx}) and (G_{yy}). The cross-spectrum is computed using the WOSA method. The time series are divided into overlapping segments which are detrended and tapered. Then a "local" cross-spectrum ($G_{xy,i}$) is calculated for each segment i as the product of the Lomb-Scargle Fourier transform of one time series (X_i) with the complex conjugate of the Lomb-Scargle Fourier transform of the second one (Y_i^*) for the same segment:

$$G_{xy,i}(f) = X_i(f)Y_i^*(f)$$

The coherency spectrum is obtained by averaging all the local cross-spectra. It is a dimensionless measure of the degree of linear relationship between two time series in the frequency domain which range from 0 (no relationship) to 1 (perfect relationship). In practice, coherency is corrected to obtain a bias-corrected coherency spectrum, since for a given frequency, the raw spectrum is greater than zero even for uncorrelated time series. This bias-corrected coherency spectrum is calculated for frequencies in the range from the fundamental frequency ($f_{fund,xy}$) to the average Nyquist frequency ($f_{Nyq,xy}$) which are obtained from the time series with the lower resolution, thus

$f_{fund,xy} = max(f_{fund,x}\,,\, f_{fund,y})$ and $f_{fund,xy} = min(f_{Nyq,x}\,,\, f_{Nyq,y})$.

Finally, it is important to note that, because the REDFIT-X program is based on the WOSA method, it therefore assumes that the analyzed signals are stationary, which is obviously not the case for our selected paleoclimatic time series in light of the results of the wavelet spectral analyses (see Results and Discussion). It is thus possible that non-stationary spectral features with close periods and time ranges that are detected in different time series using wavelets may not appear in the cross-spectral analyses using REDFIT-X.

Time series	**Number of samples**	**Minimum time (yrs cal BP)**	**Maximum time (yrs cal BP)**	**Mean time steps (yrs)**	**Age control**	**Mean age models error (years)**	**Minimum consistent period (years)**	**Degree of the polynomial trend**
Aridity Index	127	585	7719	56.17	28 ^{14}C dates and 5 historical dates	± 135	256	2
Storm Index	370	-55	7333	19.96	28 ^{14}C dates and 5 historical dates	± 135	91	5
Ca/Ti	654	41	9731	14.81	20 ^{14}C dates	± 211	68	3
K/Ti	654	41	9731	14.81	20 ^{14}C dates	± 211	68	1
Gulf of Lion SST	690	-17	9770	14.18	20 ^{14}C dates	± 211	65	4
ACL	681	-17	9760	14.35	20 ^{14}C dates	± 211	66	3
TERR-Alkanes	681	-17	9760	14.35	20 ^{14}C dates	± 211	66	3
Bay of Biscay SST	206	445	10195	47.33	10 ^{14}C dates	± 302	216	6
$\delta^{18}O$ of cave Speleothem	513	13	7783	15.14	22 U/Th	NA	69	2
ENSO variability	12301	0	11499	0.93	See Publication	NA	4	2

Table 1: General information about the analyzed time series, NA means that the value is not available.

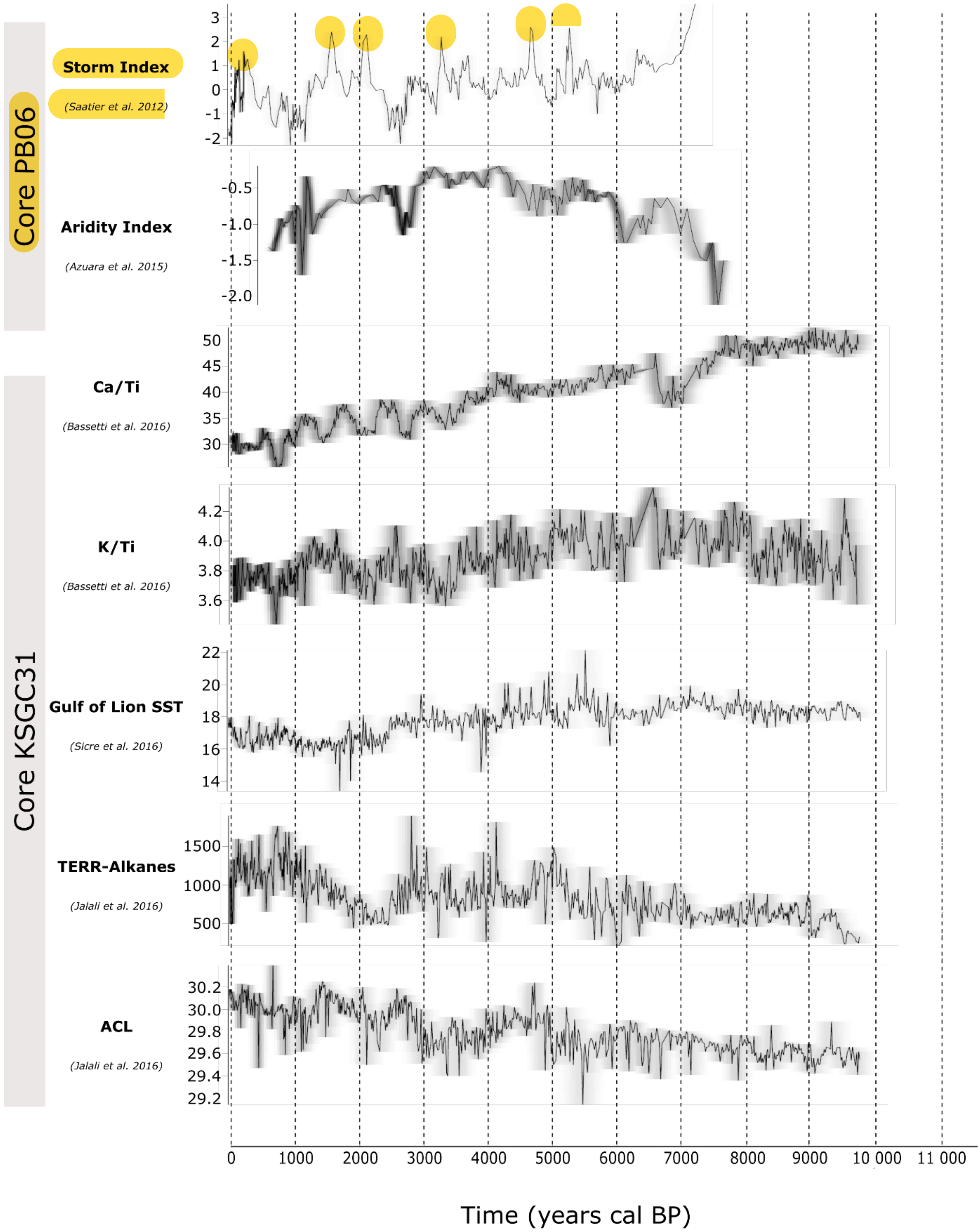

529

530 *Figure 2: Curves of the studied time series. Shaded grey area represent the age models errors of each*
531 *time series plotted using the "proxy.ghost" function of the RBACON package, darker grey indicate*
532 *more likely ages for specific proxy values.*

533

Data sets and results

This section summarizes the context, the chronological framework and the meaning of the climate proxies used in this study; it also describes briefly their main features in the frequency domain. The original curves of the Gulf of Lion sequences are presented in Figure 2 and the general characteristics of all time series are given in the Table 1 (Number of samples, length, mean time step, age control, mean age model error, minimum consistent period and degree of the polynomial trend). The detailed results of the age models error propagation are presented in a table in the Appendix 1.

PB06 core and the Palavasian lagoon system

The Palavasian lagoon system is located in southern France (Figure 1) along the coast of the Gulf of Lion. The wetland complex consists of seven shallow ponds (depth <1m) (Sabatier et al., 2008). These hypersaline, back-barrier lagoons are separated from the Mediterranean Sea by a wave-produced, sandy barrier measuring 150 m wide and rising to a height of 2–3m above the mean sea level. Tidal variability is modest (with a mean range of 0.30 m), which minimizes the influence of dynamic tidal currents. The study site is located along the southeastern-facing shoreline and is extremely vulnerable to intense storms blowing from the south and southeast (Dezileau et al. 2011).

A 7.9 m long core (PB06) was recovered from Pierre Blanche Pond in 2006 (Dezileau et al. 2011, Sabatier et al. 2010, 2012). The chronology was established using 25 Accelerator Mass spectrometry (AMS) radiocarbon dates on monospecific shell samples of Cerastoderma glaucum. The radiocarbon reservoir ages were estimated in relation to historical events and paleoenvironmental changes (Sabatier et al. 2010b). For the last centuries, historical storm events, together with short-lived radionuclide measurements, were also used (Sabatier et al. 2012).

Sedimentological analysis

Several analyses were performed on core PB06. Clay minerals were identified and quantified by X-ray diffraction (XRD) and X-ray fluorescence analyses (XRF) were also performed to estimate Al, Si, S, Cl, K, Ca, Ti, Mn, Fe, Zn, Br, Sr, Rb, and Zr contents (Sabatier et al. 2012). The macrofauna content was estimated by sieving samples at 1mm and identifying the shells every 2cm in order to identify lagoonal and marine species (Sabatier et al. 2012).

Storms are frequent in the northern Mediterranean during the wet season (October to March) and the most powerful ones are able to break the sandy barriers of coastal lagoons causing marine sediments to enter the ponds and creating what are called overwash fans as illustrated in Sabatier et al. (2008). Thus, sedimentological archives from coastal lagoons potentially represent long term records of past intense storms. Distal overwash fans are clearly identified in PB06 through the presence of marine mollusk shells (M), changes in clay mineralogy (C) and increases in the Zr/Al ratio (Z). On the basis of this sedimentological evidence, several periods of intense storm activity have been defined (Figure 2) (Sabatier et al. 2012). For the purpose of this study, all of these indicators of past storm activity were combined to sum up all of the information within one unique time series called the "Storm Index" (SI):

$$SI(t) = -C(t) + 3\times\frac{M(t)}{max(M)} + 3\times\frac{Z(t)}{max(Z)}$$

The M and Z time series are scaled by dividing them by their maxima, $max(M)$ and $max(Z)$, and then multiplying them by a factor 3 to have an amplitude of variation of about the same order of magnitude as the C time series. High SI values correspond to periods of frequent storms while low SI values correspond to periods with fewer storms.

The SI record from the Palavasian lagoon covers the last 7300 yrs with a mean temporal resolution of about 20 yrs (Table 1). After 4000 yrs cal BP, a major significant spectral feature of 1530-1590 yrs arises and continues until the end of the Holocene. Between 2500 and 1500 yrs cal BP, a significant spectral feature of 690-850 yrs is recorded. Finally, significant spectral features of 130-280 and 90-210 are recorded at around 2500 and 5500 yrs cal BP (Figure 3).

Paleoecological analysis

For pollen extraction, samples were sieved, processed with HCl and HF for mineral digestion and sodium polytungstate for density separation. Pollen concentration was estimated by adding a known amount of Lycopodium spores. Pollen grains were counted and identified at 400x and 1000x amplification, respectively, with reference to pollen keys, atlases and comparison with a reference collection (Azuara et al. 2015, 2018).

In the French Mediterranean Mountains, *Fagus sylvatica* and *Abies alba* are at the limit of their geographical range. Thus, both taxa are particularly sensitive to climate fluctuations. Decreases (increases) in pollen proportions of these two taxa synchronous with increases (decreases) in deciduous *Quercus* proportions have been interpreted as repetitive mountainous forest retreats toward higher altitudes coinciding with repeated expansions of deciduous *Quercus* at lower altitudes during dry events (Azuara et al. 2015, 2018). The covariations of these taxa are summarized within a single indicator called "Aridity index" (A_i):

$$A_i = log\left(\frac{F_p + A_p}{Q_p}\right)$$

F_p, $A_p$and Q_p are respectively *Fagus*, *Abies* and deciduous *Quercus* pollen proportions. An increase in A_i indicates increasing aridity recorded by the vegetation.

The aridity index time series ranges from 570 to 7800 yrs cal BP with a mean temporal resolution of about 60 yrs (Table 1). Before 5000 yrs cal BP, a significant spectral feature of 1180-1400 yrs prevails in the signal, while after 4000 yrs cal BP, a significant spectral feature of 1850-2120 yrs is rather recorded. Two significant spectral features of 430-700 yrs and 550-1140 yrs are recorded between 2000 and 4000 yrs cal BP (Figure 3).

KSGC-31_GolHo-1B composite core and the inner shelf of the Gulf of Lion

The KSGC-31_GolHO-1B sequence is composed of two cores retrieved from the same site on the inner shelf of the Gulf of Lion (Bassetti et al. 2016, Jalali et al. 2016, 2017) (Figure 1). In this part of the inner shelf, sediments predominantly come from the Rhône river mouth where they are advected along the coast by longshore drift thereby forming the Rhône mud belt (Bassetti et al. 2016). The chronology of the KSGC-31_GolHO-1B sequence is based on 20 AMS radiocarbon dates on mollusk shells and 210 Pb measurements. The local marine reservoir age is $\Delta R = 23 \pm 71$ years (Jalali et al. 2016, Bassetti et al. 2016).

XRF analysis

Core KSGC-31 was split into two parts and scanned with an XRF core scanner (IFREMER) to produce semi-quantitative estimates of major and minor element abundances within the sediments with a high resolution, one-centimeter step measurement. The results were expressed as element to element ratios and the resulting time series ranges from 110 to 10 050 yrs cal BP with a mean temporal resolution of about 15 yrs (Table 1, Bassetti et al. 2016).

The Ca/Ti ratio is considered to record biogenic marine productivity, marked by the Calcium abundance, versus terrigenous inputs, marked by the Titanium content. This proxy displays two main significant spectral features of 1660-1980 yrs between 4000 and 8000 yrs cal BP and 510-700 yrs after 4000 yrs cal BP, and a very short one of 170-400 yrs around 1000 yrs cal BP (Figure 3).

On the other hand, K/Ti values can be related to the transport of clay minerals, in particularly to the illite content that forms by the weathering of K-feldspars upon pedogenetic (sub-aerial) processes. The Rhône waters deliver a variable amount of illite and chlorite to the Mediterranean Sea depending on the areas of its watershed that are most eroded by precipitations. Thus, illite (K) relative abundances can be used as a proxy for sediments sources and indirectly of changes in rainfalls distribution. This time series shows one main spectral feature of 1100-1400 yrs between 5000 yrs cal BP and the present and two secondary spectral features of 590-1060 yrs between 8000-10000 yrs cal BP and 260-360 yrs cal around 6500 yrs cal BP (Figure 3).

Biomarker analysis

Biomarker analyses were performed continuously at a sampling step interval of 1 centimeter all along the sequence. Lipids were extracted from the frozen and dried sediments with dichloromethane and methanol. Alkenones and n-alkanes were isolated using silica gel chromatography and quantified using gas chromatography. The time series derived from these biomarker analyses covers the last 10 000 yrs with a mean temporal resolution of about 15 yrs (Table 1, Jalali et al. 2016).

Unsaturation ratio of C37 alkenones was converted into Sea Surface Temperature (SST) using the calibration developed by Conte et al. (2006) (Sicre et al. 2016). The weighted smoothed scalogram displays a significant spectral feature of 2120-2350 yrs from 8000 yrs cal BP to the present. Two significant spectral features of respectively 400-780 and 360-720 yrs are evident between 5500 and

6000 yrs cal BP and around 2250 yrs cal BP repsectively. Finally, a significant cyclic period of 160-300 yrs is recorded around 4500 yrs cal BP (Figure 3).

High-molecular-weight n-alkanes with an odd carbon number, i.e. C27+C29+C31+C33 homologs (TERR-alkanes), were quantified in order to track terrigenous inputs from the Rhône River (Jalali et al. 2016). Indeed, these compounds are constituents of epicuticular leaf waxes and their accumulation in the sediments of the Gulf of Lion is primarily associated with vegetation cover changes and soil erosion in the Rhône river catchment. The wavelet spectral analysis presents two major spectral features of 1910-2200 yrs between 8000 yrs cal BP and the present and 680-1260 yrs between 6000 and 2000 yrs cal BP. Then, short spectral features of 160-300 and 190-370 yrs are registered around 3000 and 7000 yrs cal BP (Figure 3).

Finally, the n-alkane Average Chain Length (ACL) was calculated between C_{27} and C_{33} in order to derive information on changing moisture conditions and associated vegetation types in the Rhône watershed (Jalali et al. 2017). Under conditions of water deficit, plants actually produce longer chain n-alkane to minimize water loss through evapo-transpiration (Gagosian and Peltzer, 1986). The weighted smoothed scalogram of the ACL time series displays a major significant spectral feature of 2520-2700 yrs between 8000 yrs cal BP and the present and another significant spectral feature of 750-1260 yrs between 4000 yrs cal BP and the present.

The speleothems of "Cueva de Asiul"

Smith et al. (2016) recovered two sequences from speleothems labeled ASR and ASM in the Cueva de Asiul, a closed karstic depression in the Cantabrian Cordillera in northwestern Spain (Figure 1). The chronologies of these sequences rely on 10 and 12 U/Th dates respectively. Speleothem ASR grew between 12500 and 500 years BP with a long interruption between 8600 and 4000 years BP. Speleothem ASM grew between 7850 and 0 yrs BP with an interruption between 3800 and 2150 years BP and thus almost entirely spans the gap in the ASR record (Smith et al. 2016 Supplementary information).

Geochemical analysis

Smith et al. (2016) performed calcite $\delta^{18}O$ analysis using an IsoPrime isotope ratio mass spectrometer to track precipitation changes throughout the Holocene. The reliability of the two records within their overlapping period was tested by cross correlation analysis and they were then combined within a single detrended time series (Smith et al. 2016 Supplementary information). The data for this combined and detrended time series were downloaded from the NOAA database for use in our study (https://www.ncdc.noaa.gov/paleo-search/study/20082).

A monitoring study in Cueva de Asiul demonstrates that the cave's hydrological system is recharged primarily by winter rainfall and that the isotopic composition of the cave drip waters reflects the $\delta^{18}O$ composition of winter rainfall from the preceding year (Smith et al. 2016 b). Therefore, $\delta^{18}O$ measurements on ASR and ASM speleothems may represent winter rather than annual past precipitation rates over the last 7800 yrs with a mean temporal resolution of 15 yrs (Table 1). The weighted smoothed scalogram of this time series displays a frequency content dominated by a spectral feature of about 1400 years between 5000 yrs cal BP and the present. Short spectral features of about 200-450 yrs are also recorded around 500, 1500, 2000 and 4500 yrs cal BP respectively (Figure 3).

The Bay of Biscay SST

Mary et al. (2017) studied the PP10-07 core recovered in the inner Bay of Biscay, at a point between the Aquitaine shelf and the Cantabrian shelf. The Bay of Biscay is characterized by a complex oceanic circulation. This area is particularly sensitive to North Atlantic subpolar and subtropical gyre dynamics. The chronology of the sequence is based on 10 AMS radiocarbon dates on planktonic foraminifera (Mary et al. 2017). The radiocarbon reservoir age is 405yrs (Reimer et al. 2013). The age model was obtained by a smooth-spline regression (Mary et al. 2017).

SST reconstructions

Mary et al. (2017) derived SSTs from the planktonic foraminifera abundances within the >150µm sediment fraction using the Modern Analogues Technique (Mary et al. 2017). The Annual SST data from the PP10-07 core were retrieved from the Pangea database to be used within our study (https://doi.pangaea.de/10.1594/PANGAEA.872166). This time series covers the last 10 000 yrs with a mean temporal resolution of 50 yrs (Table 1). Colder and warmer SST periods are recorded in the Bay of Biscay. They are related to variations in heat transport from the tropics toward Western Europe, due to changes in past dynamics of the Atlantic gyres (Mary et al. 2017).

The wavelet analysis of Bay of Biscay SSTs shows a significant spectral feature of 1049-1536 yrs throughout the first half of the Holocene. After 6000 yrs cal BP, a significant spectral feature of 1380-1890 yrs dominates the signal variability. Two short cyclic periods of 140-350 and 240-560 yrs are evidenced around 9000 and 2500 yrs cal BP (Figure 3).

Solar activity proxy

Two time series for reconstructed solar activity throughout the Holocene are available: Sunspot Number (SN) estimates from a dendro-chronologically dated ^{14}C record (Solanki et al. 2004) and Total Solar Irradiance (TSI) estimates from several cosmogenic isotope records (Steinhilber et al. 2012). Since these two time series display very similar frequency contents and since the SN time series have a better chronological framework and time resolution, it was decided to use the latter to investigate the presence of solar periodicities in the studied paleoclimate sequences (ftp://ftp.ncdc.noaa.gov/pub/data/paleo/climate_forcing/solar_variability/ solanki2004-ssn.txt).

ENSO variability

During El Niño events, high SSTs off the coast of Ecuador and northern Peru cause positive precipitation anomalies in the western Andean slope. Moy et al. (2002) studied a 9m long core from the Laguna Pallcacocha in the southern Ecuadorian Andes in which light-colored laminae of inorganic and clastic materials related to ENSO-driven episodes of alluvial deposition are recorded. This sequence spans the entire Holocene with a very high temporal resolution allowing to obtain a continuous record of the pacific climate variability over the last 12000 yrs (NOAA database : ftp://ftp.ncdc.noaa.gov/pub/data/paleo/paleolimnology/ ecuador/pallcacocha_red_intensity.txt). The age model was obtained by combining the correlation of laminae with radiocarbon dated laminae in a neighboring core and an "event model" assuming that each single high terrigenous deposition events within the core correspond to a single ENSO event. Because of the complexity of the method used to obtain this age model, it was not possible for us to propagate age model uncertainties within wavelet spectral analysis of this time series.

Red color intensity

The concentration of light-colored clastic laminae along the sequence was estimated by scanning the core with Geotek line scan camera, which generates a continuous red, green and blue digital record of the sediment surface. The red color channel was selected to document ENSO variability because it displays an higher variance than either blue and green channels.

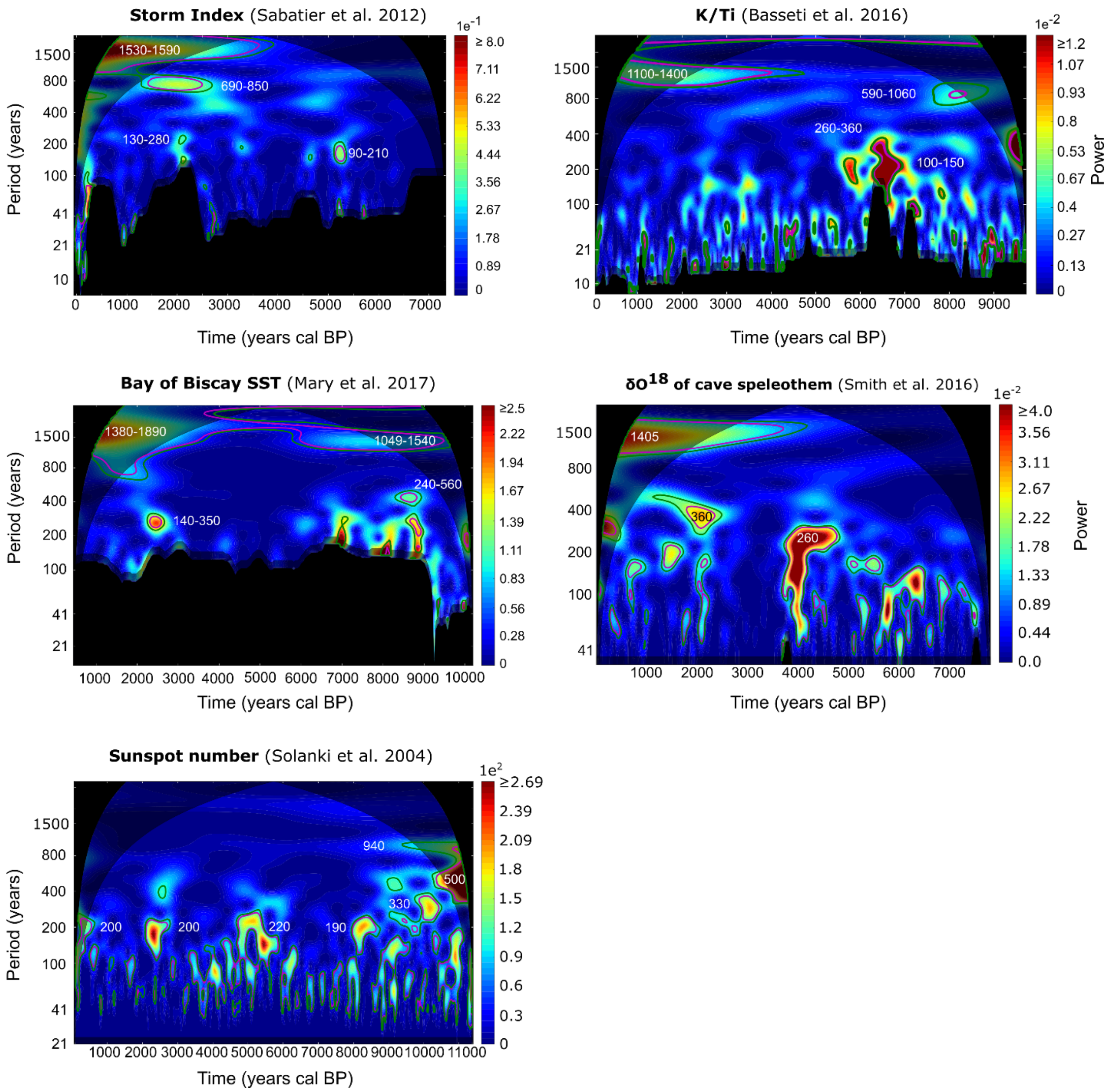

Figure 3 (part 1): Weighted smoothed scalograms of the studied time series. Colors indicate the amplitude of the wavelet power spectra, red being the highest amplitudes and blue the lowest. The purple lines represent the 95% confidence level, the green lines the 90% confidence level. The lateral grey shaded area represents the cone of influence and the lateral black areas the part of the time-scale plane excluded from the analysis because of the fixed length of integration for the smoothing of the sclalogram. The black and the grey shaded area at the bottom of each scalogram represent the SNEZ and its extension. Characteristic periods of main spectral features taking into account age model errors are reported in black or white. Since the time series differ in length and resolution, scales are different from one spectrum to another.

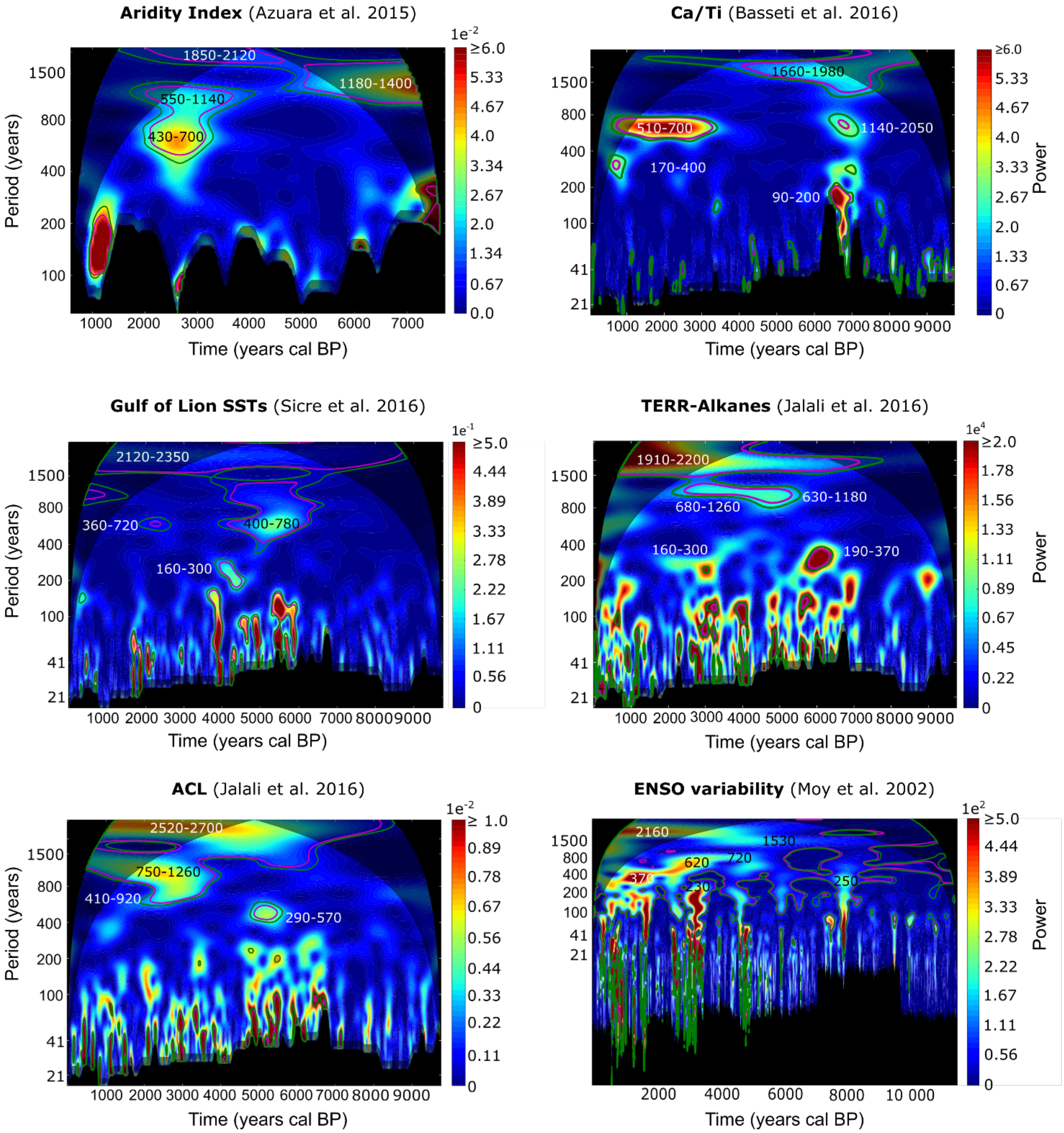

Figure 3 (part 2): see legend for Figure 3 (part 1).

Discussion

In this section, the frequency contents of each different paleoclimate proxy are compared to one another in order to better understand Holocene climate variability and its underlying mechanisms.

Oceanic forcing? The 1500 yrs cyclic period

SI, and K/Ti ratio time series from the Gulf of lion on one hand and speleothem $\delta^{18}O$ and Bay of Biscay SST time series from the near Atlantic area on the other hand, display similar significant spectral features after 5000 yrs cal BP characterized by periods of respectively 1530-1590, 1100-1400, 1405 and 1380-1890 yrs (Figure 3). This low frequency periodicities are also significantly recorded using REDFIT program (Appendix 1). The coherency spectra of Gulf of Lion time series with Atlantic ones confirm that they are indeed significant shared spectral features, except in the case of the K/Ti ratio and the Bay of Biscay SST in which a marked but non-significant spectral peak at 1500 yrs is detected (Figure 4). These results highlight a link between the climate of the Atlantic area and the Gulf of Lion. The comparison of these sequences filtered with a 1450-1550 yrs passband filter highlights time intervals of high (or low) storm activity in the Gulf of Lion that correspond to lower (or higher) precipitation in northwestern Spain and cooler (or warmer) SSTs in the Bay of Biscay since 5000 yrs cal BP (Figure 5). The oscillations also visible in the K/Ti ratio are more difficult to interpret. Insofar, as this proxy is an indicator of the sediments source, these fluctuations must be linked to changes in precipitation regime within the Rhone watershed causing changes of eroded areas. The time series are slightly off-set from each other, but these discrepancies are consistent with the order of magnitude of the age models' uncertainties (Table 1).

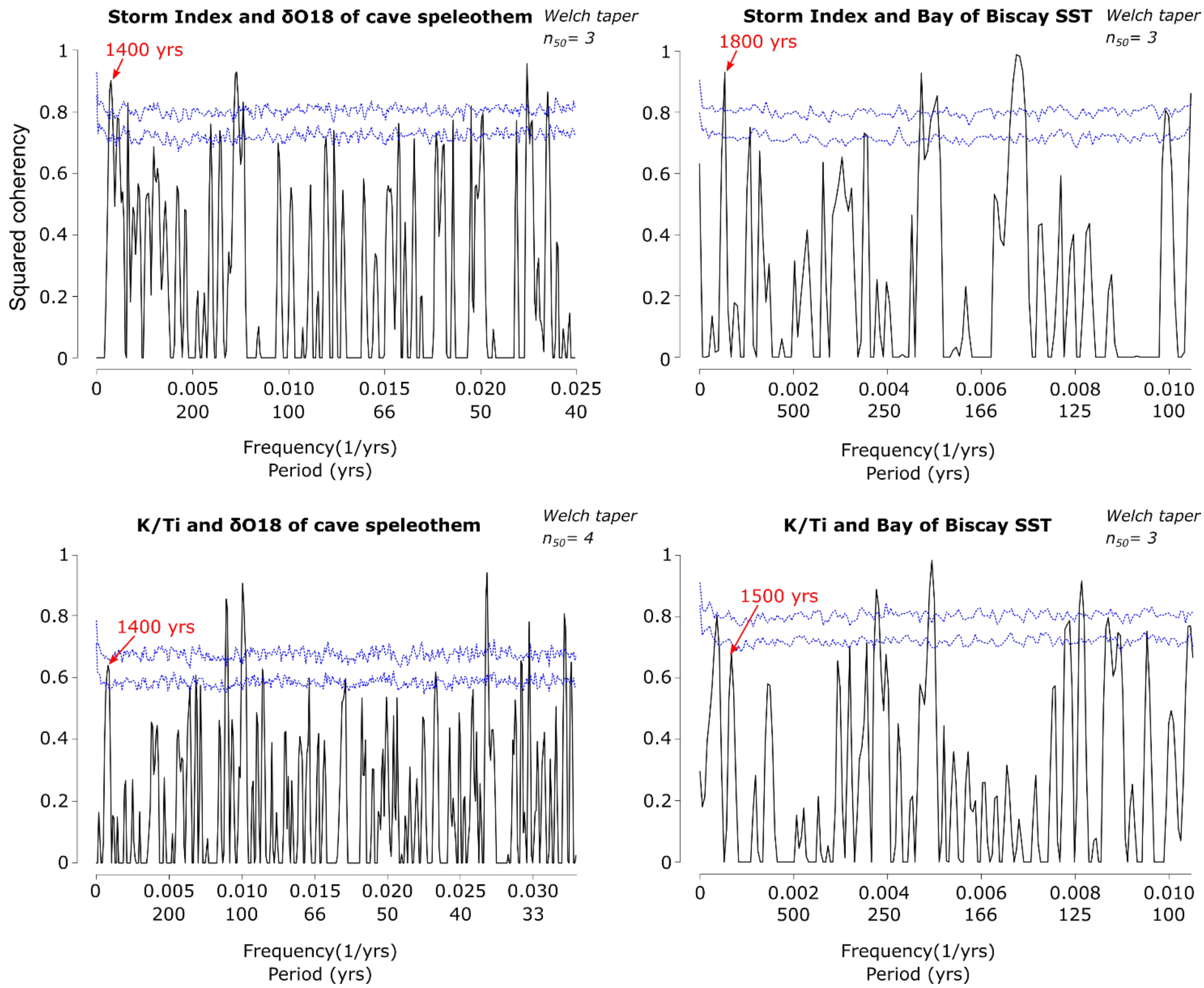

Figure 4: Coherency spectrum of the Palavas Storm Index and K/Ti ratio time series with the Atlantic paleoclimatic proxies, Cave speleothem $\delta^{18}O$ and Bay of Biscay SST. The dashed blue lines represent the 0.90 and 0.95 confidence levels and the spectral peaks of interest are pointed with a red arrow.

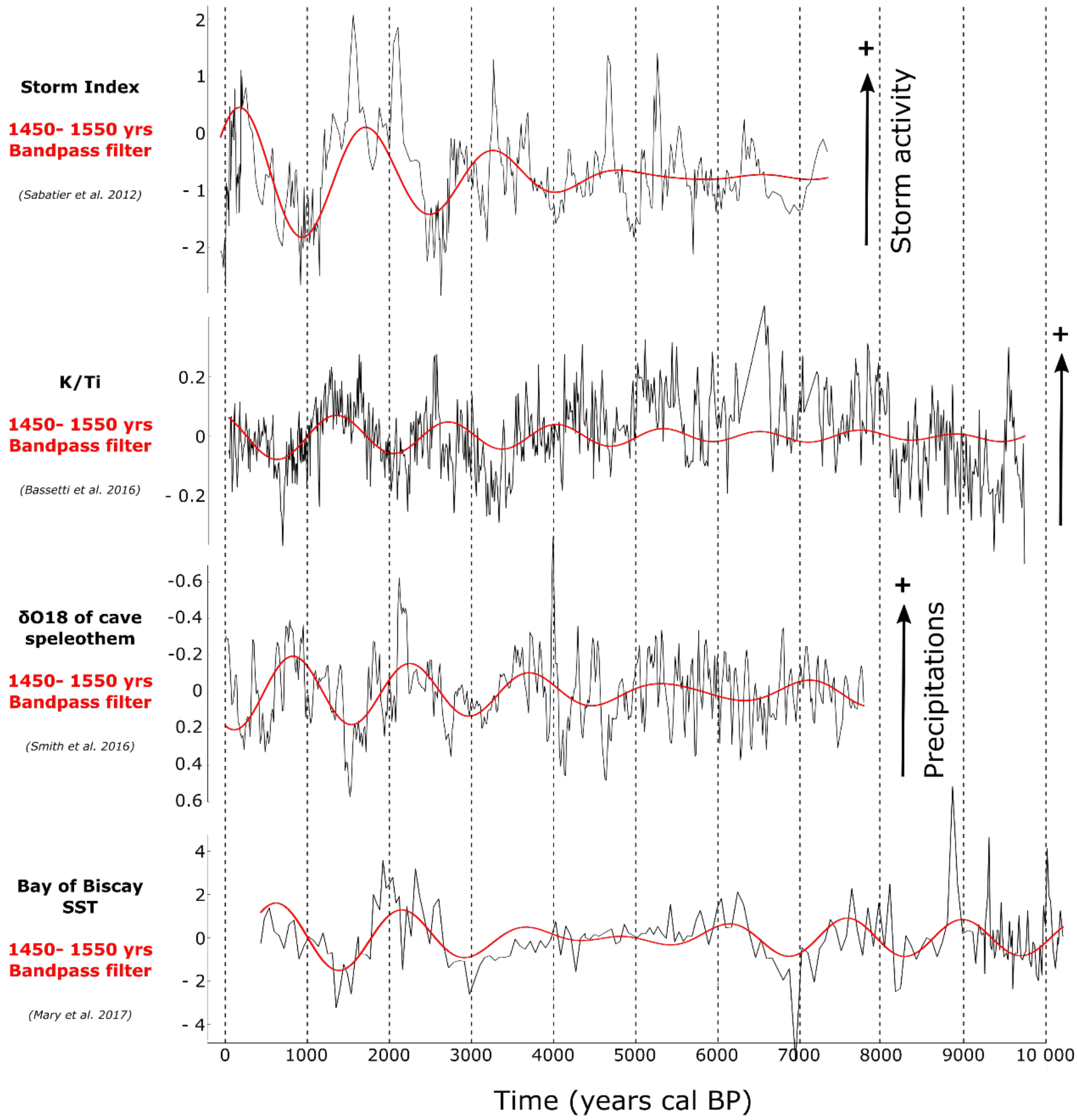

Figure 5: Comparison of the Palavas Storm Index (SI), the K/Ti ratio from the Gulf of Lion, the Asiul Cave speleothem $\delta^{18}O$, and the Bay of Biscay SSTs filtered with a 1450-1550 yrs bandpass filter to highlight variations linked to the ~1500 yrs cycles. The Bay of Biscay SSTs record from the PP 10-07 core (dashed blue curve, Mary et al. 2017) studied in this article is completed here with the SSTs record from the MD03-2693 core (dashed green curve, Mary et al. 2015) to show the important decrease in Bay of Biscay SSTs at the last part of the sequence.

Such ~1500 oscillations were first characterized by Bond et al. (2001) within stacked Ice Rafted Debris (IRD) records from the north Atlantic. Nevertheless, their gradual appearance during the second part of the Holocene and thus their non-stationarity, was first described by Debret et al. (2007) in several North Atlantic climate proxies including Bond's stacked IRD time series. Based on the predominance of this pattern in proxies specifically recording water mass activity in the Atlantic, Debret et al. (2007, 2009) assumed that this variability reflected changes in the Atlantic thermohaline circulation. The detection of a similar cyclic period in the Bay of Biscay SSTs, which depend on the dynamics of Atlantic gyres, supports this hypothesis and further implies that these changes affect both deep and surface Atlantic waters. On the other hand, this ~1500 yrs variability is also evidenced in proxies related to mid-latitude atmospheric circulation. Indeed, such cycles are also recorded in a storminess record from north-western Europe (Sorrel et al 2012) in phase with the high storm activity periods registered in the Gulf of Lion (Sabatier et al. 2012). Moreover, the speleothem $\delta^{18}O$ from northwestern Spain, which also displays these cycles, is related to advection of Atlantic low-pressure systems over the Iberian Peninsula. Thus, if internal fluctuations of the Atlantic thermohaline circulation are actually responsible for these late Holocene ~1500 years cyclic period, what mechanism might explain the fact that this frequency pattern also affects past atmosphere dynamics?

Experiments using ocean/atmosphere coupled models show an influence of the Atlantic Meridional Overturning Circulation (AMOC) on Atlantic storm track strength and position during winter time (Brayshaw et al. 2009, Woolings et al. 2012, Harvey et al. 2015). The Atlantic storm track is an area where depressions form preferentially and travel down the prevailing winds. Its strength corresponds to the number and the importance of the lows formed during a given period and is quantified using the variance of the Mean Sea Level Pressure (MSLP). In models, AMOC weakening causes a strengthening of the storm track which spreads eastwards over northern Europe (Figure 6). The weaker heat transport from the tropics toward the pole, because of the AMOC slowdown, induces cooler SSTs in the North Atlantic and increases sea ice extent in the Arctic. The resulting increase in the mid-latitude temperature gradient causes an increase in baroclinicity and thus cyclogenesis (Raible et al. 2007, Brayshaw et al. 2009, Woolings et al. 2012, Harvey et al. 2015). This mechanism would explain why a periodic weakening of the AMOC induces lower SSTs in the Bay of Biscay and causes an increase in storminess in northwestern Europe (Sorrel et al. 2012) by a direct increase in the number of depressions advected over this area.

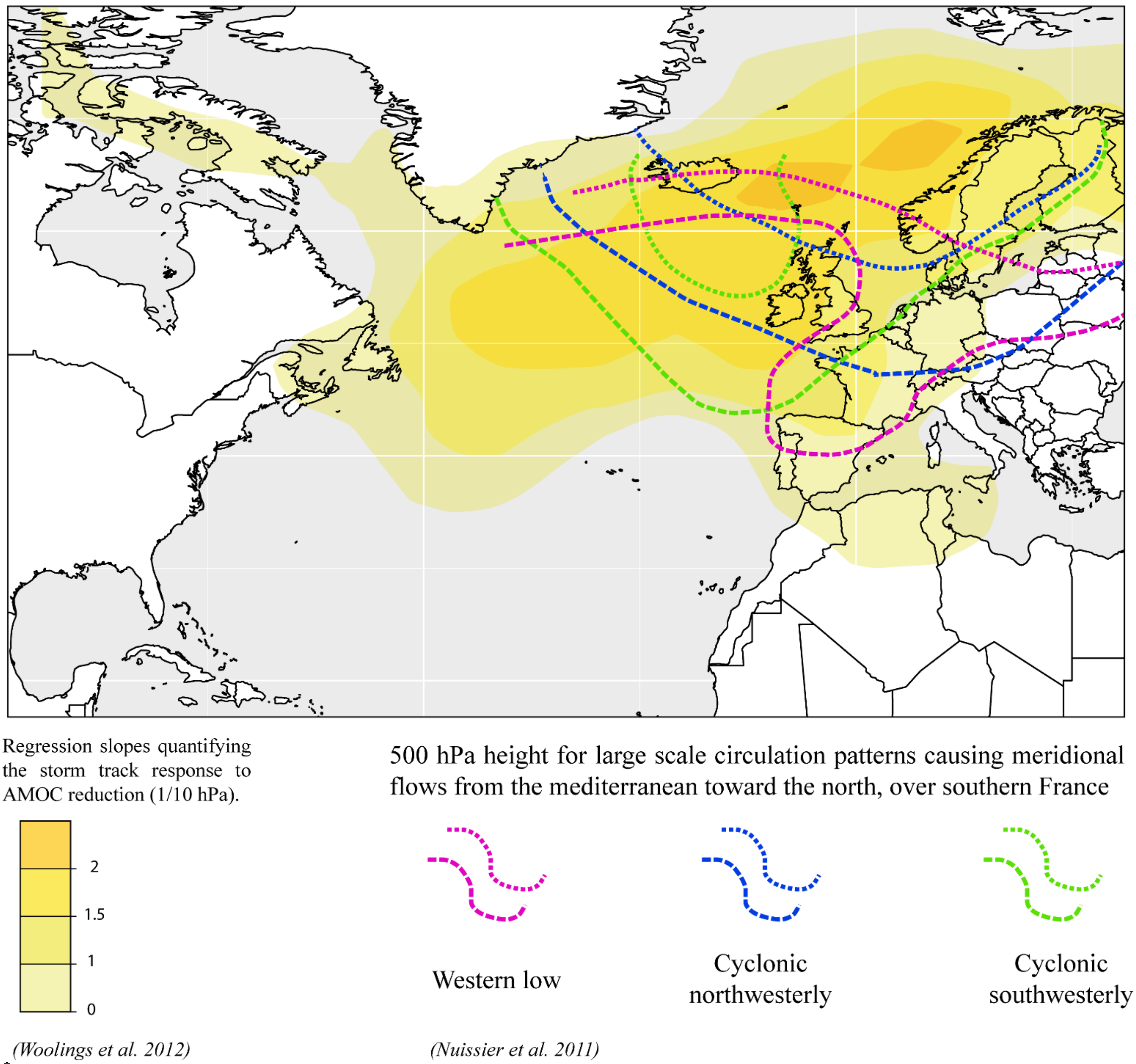

Figure 6: Comparison of the storm track response to AMOC reduction in experimental models (Woolings et al. 2012) and position of the lows during large scale circulation patterns which cause Mediterranean air masses to flow northwards over southern France, thereby perhaps leading to higher storm frequencies in the Gulf of Lion (Nuissier et al. 2011).

In the Gulf of Lion, heavy precipitation events and marine storms are both linked to the northward flow of warm, moist air masses from the Mediterranean, bringing humidity over areas of high relief and associated with very strong south-easterly to south-westerly winds (>40 $m.s^{-1}$) in the case of marine storms (Sabatier et al. 2008). Nuissier et al. (2011) identified the different Large-Scale Circulation patterns (LSC) leading to such northward flows of Mediterranean air masses by analyzing meteorological data for wintertime between 1960 and 2000. The 500 hPa heights describing the altitude pressure field of these LSCs are reported on the map showing the response of the Atlantic storm track to AMOC weakening (Figure 6). The area of enhanced storm track strength encompasses the location of the low-pressure systems which could induce heavy precipitations and storms in the Gulf of Lion. Therefore, repetitive weakening of the AMOC, which strengthens the Atlantic storm track, could also explain the ~1500 yrs spectral feature evident in the Palavas SI. Regarding the fluctuations in the K/Ti ratio, it is possible that the periods of greater storm frequency also have caused a greater sediments contribution from the southern part of the Rhone watershed due to more frequent heavy precipitation events. However, further studies are necessary to test this hypothesis.

Finally, Brayshaw et al. (2009) highlight the fact that a weakening of the AMOC can cause a decrease in winter precipitation over all of Western Europe, including the western Mediterranean area. Indeed, the SST reduction over the North Atlantic reduces the saturation water vapor pressure. Thus, despite the stronger zonal flow, the air masses from the Atlantic advected over Western Europe are cooler and drier. Since the speleothem $\delta^{18}O$ from northwestern Spain probably records winter precipitation in a region that is very sensitive to Atlantic influences (Smith et al. 2016), it makes sense that high storm activity periods are associated with lower precipitation in the northern Iberian Peninsula. Especially since more frequent storms and heavy precipitation events in the Gulf of Lion are linked to the advection of moisture-laden northward air masses originating from the Mediterranean and not eastward air masses from the Atlantic (Nuissier et al. 2011).

All of this evidence is consistent with several weakening of the AMOC during the latter part of the Holocene. Such variations are consistent with the well-known Bond events evident in North Atlantic IRD records (Bond et al. 2001). Sgubin et al. (2017) highlight that an important proportion (45.5%) of global climate models, which reproduce more accurately the structure of the North Atlantic Ocean, are predicting an imminent local collapse of the deep ocean convection in the Labrador Sea linked to the ongoing climate change. This possible interruption of deep-water formation could be similar to periodic weakening of the AMOC. Therefore, understanding the cause and the mechanism of such millennial scale climate variability appears crucial to improve our ability to predict the future climate.

Solar forcing: 210 yrs cyclic periods

The two short spectral features of about ~200 yrs displayed in the SI time series around 2500 and 5500 yrs cal BP (Figure 3) look similar in term of period and time interval to the 210 yrs so called De Vries cycles evidenced in solar activity proxies (Figure 6) (Stuiver and Braziunas 1989, Debret et al. 2007, Ma 2007, Debret et al. 2009, Steinhilber et al. 2012, Usokin et al. 2016). The possibility of shared spectral features between Gulf of Lion storminess records and solar variability proxies is further supported by a ~270 yrs periodicity found within a storminess record spanning the last 3000 yrs from the Bagnas pond, located about 40 km from Palavas, (Degeai et al. 2016). However, we were not able to detect any significant shared spectral features corresponding to De Vries cycles in the SI time series using coherency analyses. This is not surprising since the De Vries cycles are highly non-stationary and the WOSA algorithm on which the REDFITX consistency analyses are based assumes a stationary signal. Nevertheless, it makes it difficult to draw any conclusions. Several studies conducted in Europe and in the Mediterranean also provide evidence for increases in precipitation and flood frequencies related to centennial scale solar variability (Wirth et al. 2013, Czymzik et al. 2016, Sabatier et al. 2017, Zielhofer et al. 2017). Results suggest that centennial scale changes in solar irradiance strongly affect atmospheric circulation in the European Atlantic sector inducing NAO-like variability (Raible et al. 2007, Martin-Puertas et al. 2012). However, for now, no reliable reconstructions of the past NAO variability covering the entire Mid and Late Holocene period is available (Ortega et al. 2015, Franke et al. 2017). Thus, further work is needed to better address this issue.

ENSO influences?

The major changes in SST and atmospheric surface pressures characterizing the ENSO variability in the tropical Pacific, also affect climate variability at higher latitudes in very remote parts of the globe (Brönnimann et al. 2007). Many studies relying on instrumental data (Loon and Madden, 1981; Fraedrich 1990, 1994; Fraedrich and Müller,1992; May and Bengtsson, 1998; Mariotti et al. 2002; Xoplaki 2002 ; Gouirand and Moron, 2003; Moron and Gouirand, 2003; Muñoz-Diaz and Rodrigo, 2005; Mariotti et al. 2005; Pozo-Vazquez et al. 2005) and on experiments based on Ocean-atmosphere coupled models (Raible et al. 2001, 2004; Deser et al. 2006; Brönnimann et al. 2007) support a non-stationary but significant influence of ENSO variability on Western Europe including the Western Mediterranean. Such remote influence of the pacific area on the European climate is further supported by results from climate reconstructions over the last centuries (Mann et al. 2000, Rimbu et al. 2003, Brönnimann et al. 2007, Balting et al. 2020). Therefore, in this section our attention focuses on the potential influence of ENSO variability on the northwestern Mediterranean climate throughout the mid- to late Holocene.

To address this issue, the frequency content of western Mediterranean paleoclimate sequences was compared with the frequency content of a high-resolution ENSO variability record from the Ecuadorian Andes spanning the Holocene (Moy et al. 2002) (Figure 3).

The ENSO variability record shows some interesting spectral features which might correspond to unattributed ones in our Mediterranean sequences (Figure 3). In the ENSO time series, the significant spectral feature with a period of 620 yrs between 2000 and 4000 yrs cal BP, gradually changing to a period of 720 yrs between 4000 and 6000 yrs cal BP (Figure 3) remind the following significant spectral features in Mediterranean sequences:

i. 430-700 yrs between 2000 and 3000 yrs cal BP (AI)

ii. 510-700 yrs between 1000 and 3000 yrs cal BP (Ca/Ti)

iii. 360-720 yrs around 2000 yrs cal BP and 400-780 yrs between 4000 and 6000 yrs cal BP (Gulf of Lion SST)

iv. 630-1260 yrs between 2000 and 5000 yrs cal BP (TERR-Alkanes)

These similarities are confirmed by the coherency analyses with the ENSO variability time series which all display a significant spectral peak around 600 yrs for AI, Ca/Ti and Gulf of Lion SST and around 750 yrs for TERR-Alkanes (Figure 7).

In a similar way, the ENSO ~2160 yrs significant spectral feature between the present and 6000 yrs cal BP (Figure 3) remind the following significant spectral features in the Mediterranean sequences:

i. 1850-2120 yrs between 1000 and 5000 yrs cal BP (AI)

ii. 2120 -2350 yrs between the present and 6000 yrs cal BP (Gulf of Lion SST)

iii. 1910-2190 yrs between the present and 7000 yrs cal BP (TERR-Alkanes)

Again, these similarities are confirmed by coherency analyses with the ENSO time series which display significant peaks around 2300 (AI), 2500 (Gulf of Lion STT) and 2000 yrs (TERR-Alkanes) (Figure 7).

Finally, coherency analyses between the ENSO variability and AI and Ca/Ti time series allow to highlight significant peaks around 350 and 325 yrs while coherency analyses with Gulf of Lion SST and TERR-Alkanes time series display significant peaks around 280 yrs (Figure 7). However, the comparison of the scalograms of these times series show that these significant peaks may be spurious shared features related to the violation of the hypothesis of stationarity since all these signals displays more or less marked spectral features around periods of 300 yrs in wavelet spectral analyses, however they never occurred at the same time as in the ENSO signal.

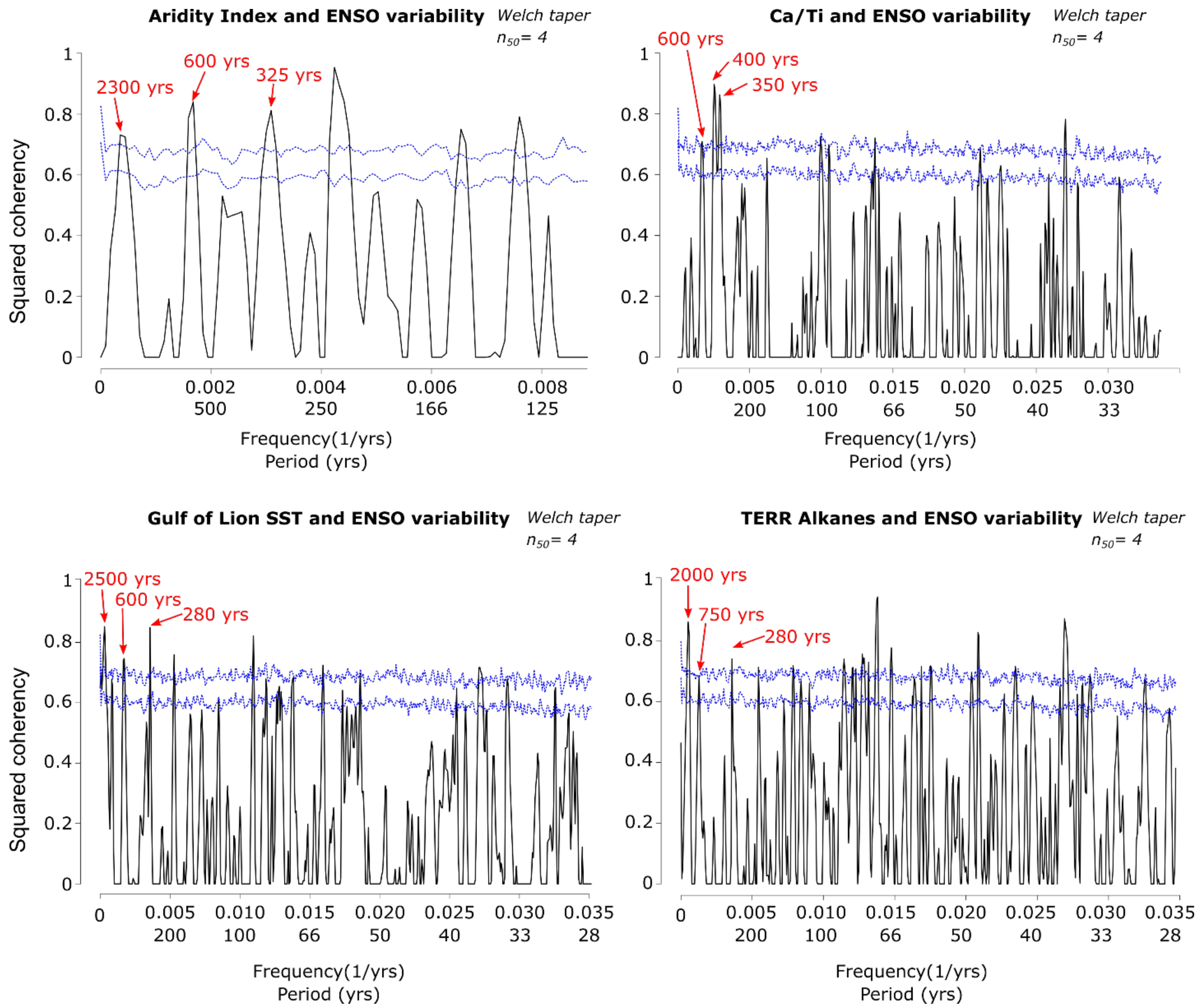

Figure 7: *Coherency spectrum of the Palavas Aridity Index, the Ca/Ti ratio, the Gulf of Lion SST and the TERR-Alkanes time series with the ENSO variability proxy. The dashed blue lines represent the 0.90 and 0.95 confidence levels and the spectral peaks of interest are pointed with a red arrow.*

The comparison of these sequences filtered with 600-700 and 2000-2200 yrs passband filters clearly show that these shared spectral features play a major role in the millennial and centennial scale variability of these time series (Figure 8). Moreover, these results highlight the remarkable similarities of the ENSO variability time series with the TERR-Alkanes and the Gulf of Lion SST. Periods of higher ENSO variability clearly correspond to periods of enhanced erosion and thus probably enhanced rainfall in southern France, as well as periods of higher SST in the Gulf of Lion (Figure 8). On the other hand, the AI and Ca/Ti time series do not show any obvious similarities with ENSO variability apart from the spectral signatures already discussed. It is very interesting to note that these shared periodicities arise during the second part of the Holocene after 5000 yrs cal BP simultaneously with a regime shift toward a dynamics characterized by more frequent and stronger EL Niño events (Tsonis 2009).

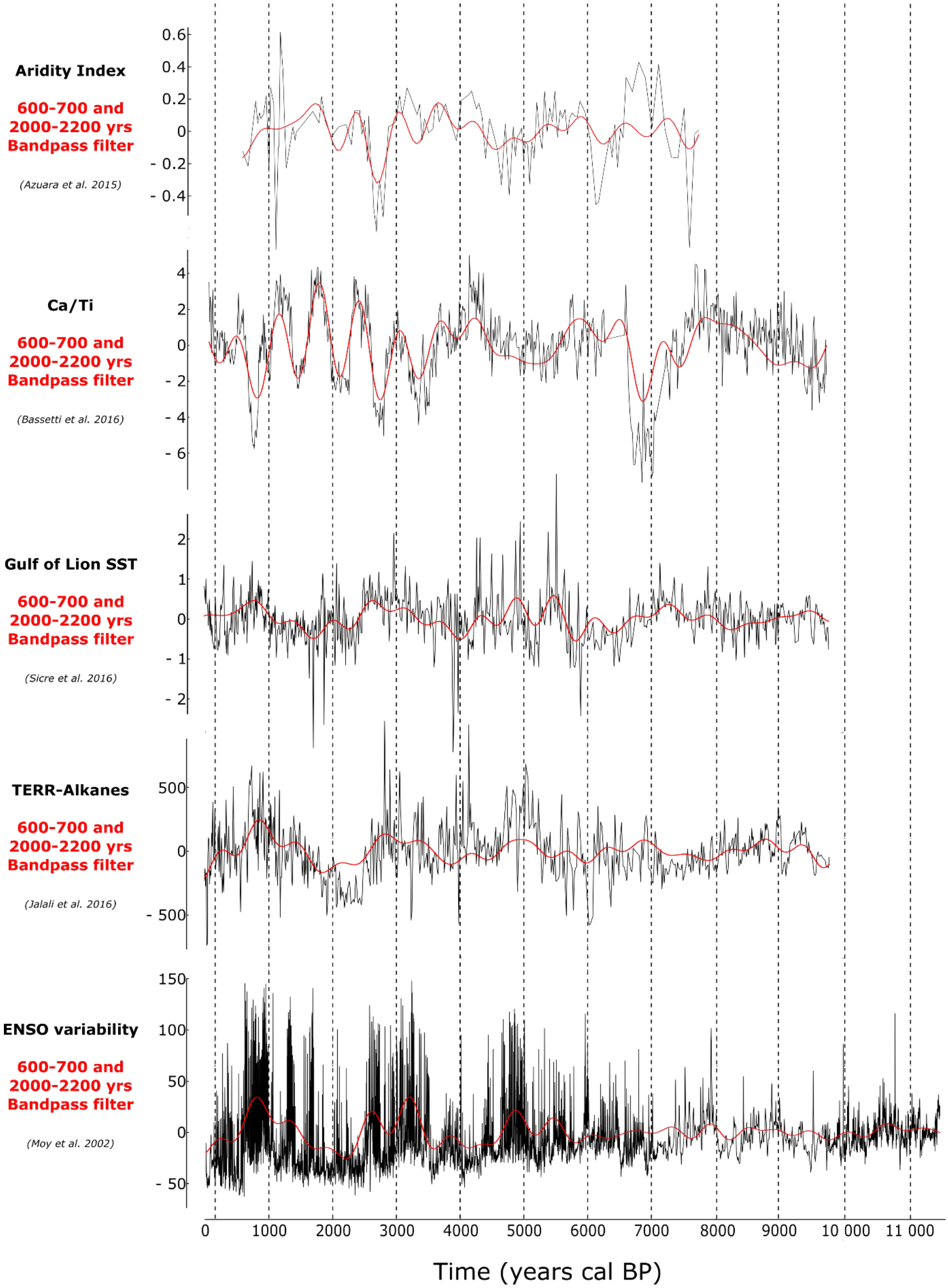

Figure 8: Comparison of the Aridity Index (SI), the Ca/Ti ratio, the Gulf of Lion SST, the TERR-Alkane and the ENSO variability time series filtered with 600-700 and 2000-2000 yrs bandpass filter to highlight variations linked to the shared spectral features detected in these sequences.

One of the mechanisms explaining such a remote connection between the past climate variability in the Pacific area and the western Mediterranean that has been most studied, involves a downstream propagation of ENSO impact along a North-Pacific/North-Atlantic connection during boreal winters. The season-averaged mid-latitude atmospheric circulation can be broken down into two components: (i) the zonal mean flow and (ii) asymmetric features arising from irregularities of the earth's surface (mountains, continent-ocean contrast, sea surface temperature asymmetries, etc.) referred to as stationary waves (Held et al. 2002, Nigam and DeWeaver, 2003). During boreal winters, when the amplitude of these stationary waves is maximal in the Northern Hemisphere (Nigam and DeWeaver, 2003), the ENSO events may change their structure by disrupting Hadley's circulation (Brönnimann et al. 2007). Such a change of the quasi-stationary wave over the north Atlantic can impact, among other things, on the cyclogenesis of this area, the Icelandic low, the Azores high and the NAO variability (e.g. Cassou and Terray, 2001, Honda et al. 2001, Raible 2001, Moron and Gouirand 2003). ENSO could also affect European climate through a downward propagation of stratospheric anomalies (e.g. Randel, 2004; Manzini et al. 2006).

Further research is needed to better understand the relative importance of the different Pacific/Atlantic coupling mechanisms, and the link between ENSO and European climate at the decadal and multidecadal scale (Brönnimann et al. 2007). However, our results and the studies mentioned above make the ENSO influence a credible hypothesis to explain the similarities between records in the north-western Mediterranean and those in the eastern Pacific. On the other hand, the shared spectral features between the tropical Pacific and the western Mediterranean time series could also arise from an independent climate forcing, which might influence both ENSO and the Mediterranean variability without implying any direct link between them. This could be particularly the case for the significant spectral feature of period ~2200 yrs recorded during the second half of the Holocene in the ENSO, AI Gulf of Lion SST and TERR-alkanes time series. Indeed, it reminds 2100-2400 yrs periodicity (Hallstatt cycles) discussed in solar activity proxies but that we haven't been able to detect significantly neither with wavelet spectral analysis nor with the WOSA algorithm (Figure 3 and Appendix 1) (Stuiver and Braziunas 1989, Debret et al. 2007, Ma 2007, Debret et al. 2009, Steinhilber et al. 2012, Usokin et al. 2016). Thus, further investigation is needed to accurately address the question of the potential influence of ENSO variability on the north-western Mediterranean climate throughout the Holocene. However, a review of the frequency content of a full set of paleoclimatic time series from the tropical areas in order to investigate this issue is a huge task beyond the scope of this article.

Conclusion

Seven paleoclimate time series from the Gulf of Lion, together with time series recording the Atlantic climate and ENSO past variability, were compared in the frequency domain using wavelet analysis for irregularly sampled signals. Since direct comparison of all of their oscillations is not informative, the comparison of their frequency content is used to discuss directly the forcing and mechanism underlying Mediterranean climate variability. Indeed, two groups of shared spectral features may be defined on the basis of the results of our analysis: (i) an Atlantic spectral feature of ~1500 yrs since 5000 yrs cal BP, and (ii) tropical Pacific spectral features of 600-700 and ~2100 yrs recorded respectively around 2500, and during the second part of the Holocene. The Atlantic cyclic period of ~1500 yrs is probably related to repetitive fluctuations of the Atlantic thermohaline circulation which induces changes in the storm track extension and position, with impacts on both precipitation and storminess in the Gulf of Lion over millennial scale. On the other hand, the tropical Pacific features recorded in many climate proxies from the Gulf of Lion, might highlight the influence of the ENSO climate variability over the western Mediterranean.

Of course, further studies are needed to fully characterize and understand Mediterranean climate variability during the Holocene period. However, it is interesting to note that the Altantic paleoclimatic variability, which is often considered as one of the main factors influencing past Western Mediterranean climate, is clearly detected in only two of the seven proxies analyzed while possible tropical features are clearly highlighted. The link between the tropical latitudes and the Mediterranean Basin needs to be better characterized. One might also wonder to what extent the leading mechanisms of climatic change described here influence and control climatic variability in the Eastern Mediterranean, considering the east-west see-saw pattern described by Roberts et al. (2012). We might also ask whether the described patterns are valid in the southern Mediterranean realm, given the north-south paleohydrological contrast reported by Magny et al. (2013). Nevertheless, the results presented in this review article establish a state of the art for paleoclimate variability in the north-western Mediterranean area. Wavelet spectral analyses allows us to understand the “natural” millennial and centennial scale variability of the earth’s climate system in this climatic change hot spot (Giorgi, 2006).

Acknowledgements

This research was funded by MISTRALS/PALEOMEX meta-program, the CNRS and the French Museum of National History (MNHN). Paleoclimate time series were extracted from the PANGEA and the NOAA database and the work of the data contributors and the PANGEA and NOAA communities is gratefully acknowledged. None of the authors have conflicts of interest to declare. The crew operating the GMO2-Carnac (R/V *Le Suroît* retrieving core KSGC31) and GolHo (R/V *Néréis*) cruises are thanked.

References

Alley, R.B., Mayewski, P.A., Sowers, T., Stuiver, M., Taylor, K.C., Clark, P.U., 1997. Holocene climatic instability: A prominent, widespread event 8200 yr ago. Geology 25, 483–486.

Anchukaitis, K.J., Tierney, J.E., 2013. Identifying coherent spatiotemporal modes in time-uncertain proxy paleoclimate records. Climate Dynamics 41, 1291–1306. https://doi.org/10.1007/s00382-012-1483-0

Azuara, J., Combourieu-Nebout, N., Lebreton, V., Mazier, F., Müller, S.D., Dezileau, L., 2015. Late Holocene vegetation changes in relation with climate fluctuations and human activity in Languedoc (southern France). Climate of the Past 11, 1769–1784. https://doi.org/10.5194/cp-11-1769-2015

Azuara, J., Lebreton, V., Peyron, O., Mazier, F., Combourieu-Nebout, N., 2018. The Holocene history of low altitude Mediterranean Fagus sylvatica forests in southern France. Journal of Vegetation Science 29, 438–449.

Balting, D.F., Ionita, M., Wegmann, M., Helle, G., Schleser, G.H., Rimbu, N., Freund, M.B., Heinrich, I., Caldarescu, D., Lohmann, G., 2020. Large scale climate signals of a European oxygen isotope network from tree-rings – predominantly caused by ENSO teleconnections? Climate of the Past Discussions 1–24. https://doi.org/10.5194/cp-2020-39

Bar-Matthews, M., Ayalon, A., 2011. Mid-Holocene climate variations revealed by high-resolution speleothem records from Soreq Cave, Israel and their correlation with cultural changes. The Holocene 21, 163–171. https://doi.org/10.1177/0959683610384165

Bassetti, M.-A., Berné, S., Sicre, M.-A., Dennielou, B., Alonso, Y., Buscail, R., Jalali, B., Hebert, B., Menniti, C., 2016. Holocene hydrological changes in the Rhône River (NW Mediterranean) as recorded in the marine mud belt. Climate of the Past 12, 1539–1553. https://doi.org/10.5194/cp-12-1539-2016

Billeaud, I., Tessier, B., Lesueur, P., 2009. Impacts of late Holocene rapid climate changes as recorded in a macrotidal coastal setting (Mont-Saint-Michel Bay, France). Geology 37, 1031–1034.

Blaauw, M., 2010. Methods and code for 'classical'age-modelling of radiocarbon sequences. quaternary geochronology 5, 512–518.

Blaauw, M., Christen, J.A., 2011. Flexible paleoclimate age-depth models using an autoregressive gamma process. Bayesian analysis 6, 457–474.

Bond, G., 2001. Persistent Solar Influence on North Atlantic Climate During the Holocene. Science 294, 2130–2136. https://doi.org/10.1126/science.1065680

Bond, G., 1997. A Pervasive Millennial-Scale Cycle in North Atlantic Holocene and Glacial Climates. Science 278, 1257–1266. https://doi.org/10.1126/science.278.5341.1257

Bout-Roumazeilles, V., Combourieu-Nebout, N., Desprat, S., Siani, G., Turon, J.-L., Essallami, L., 2013. Tracking atmospheric and riverine terrigenous supplies variability during the last glacial and the Holocene in central Mediterranean.

Brayshaw, D.J., Woollings, T., Vellinga, M., 2009. Tropical and Extratropical Responses of the North Atlantic Atmospheric Circulation to a Sustained Weakening of the MOC. Journal of Climate 22, 3146–3155. https://doi.org/10.1175/2008JCLI2594.1

Brönnimann, S., Xoplaki, E., Casty, C., Pauling, A., Luterbacher, J., 2007. ENSO influence on Europe during the last centuries. Climate Dynamics 28, 181–197.

Bueh, C., Nakamura, H., 2007. Scandinavian pattern and its climatic impact. Quarterly Journal of the Royal Meteorological Society 133, 2117–2131.

Cassou, C., Terray, L., 2001. Dual influence of Atlantic and Pacific SST anomalies on the North Atlantic/Europe winter climate. Geophysical research letters 28, 3195–3198.

Cassou, C., Terray, L., Phillips, A.S., 2005. Tropical Atlantic influence on European heat waves. Journal of climate 18, 2805–2811.

Cazelles, B., Chavez, M., Berteaux, D., Ménard, F., Vik, J.O., Jenouvrier, S., Stenseth, N.C., 2008. Wavelet analysis of ecological time series. Oecologia 156, 287–304.

Chamley, H., 1971. Recherches sur la sédimentation argileuse en Méditerranée. Persée-Portail des revues scientifiques en SHS.

Combourieu Nebout, N., Peyron, O., Dormoy, I., Desprat, S., Beaudouin, C., Kotthoff, U., Marret, F., 2009. Rapid climatic variability in the west Mediterranean during the last 25 000 years from high resolution pollen data. Climate of the Past 5, 503–521.
Conte, M., Giuffrida, A., Tedesco, S., 1989. Mediterranean Oscillation: Impact on Precipitation and Hydrology in Italy, in: Conference on Climate and Water.
Conte, M.H., Sicre, M.-A., Rühlemann, C., Weber, J.C., Schulte, S., Schulz-Bull, D., Blanz, T., 2006. Global temperature calibration of the alkenone unsaturation index (UK′ 37) in surface waters and comparison with surface sediments. Geochemistry, Geophysics, Geosystems 7.
Costas, S., Naughton, F., Goble, R., Renssen, H., 2016. Windiness spells in SW Europe since the last glacial maximum. Earth and Planetary Science Letters 436, 82–92.
Czymzik, M., Muscheler, R., Brauer, A., 2016. Solar modulation of flood frequency in central Europe during spring and summer on interannual to multi-centennial timescales. Climate of the Past 12, 799–805.
Debret, M., Bout-Roumazeilles, V., Grousset, F., Desmet, M., McManus, J.F., Massei, N., Sebag, D., Petit, J.-R., Copard, Y., Trentesaux, A., 2007. The origin of the 1500-year climate cycles in Holocene North-Atlantic records. Climate of the Past Discussions 3, 679–692.
Debret, M., Sebag, D., Crosta, X., Massei, N., Petit, J.-R., Chapron, E., Bout-Roumazeilles, V., 2009. Evidence from wavelet analysis for a mid-Holocene transition in global climate forcing. Quaternary Science Reviews 28, 2675–2688. https://doi.org/10.1016/j.quascirev.2009.06.005
Degeai, J.-P., Devillers, B., Dezileau, L., Oueslati, H., Bony, G., 2015. Major storm periods and climate forcing in the Western Mediterranean during the Late Holocene. Quaternary Science Reviews 129, 37–56. https://doi.org/10.1016/j.quascirev.2015.10.009
deMenocal, P., Ortiz, J., Guilderson, T., Adkins, J., Sarnthein, M., Baker, L., Yarusinsky, M., 2000. Abrupt onset and termination of the African Humid Period:: rapid climate responses to gradual insolation forcing. Quaternary science reviews 19, 347–361.
Deser, C., Capotondi, A., Saravanan, R., Phillips, A.S., 2006. Tropical Pacific and Atlantic climate variability in CCSM3. Journal of Climate 19, 2451–2481.
Dezileau, L., Pérez-Ruzafa, A., Blanchemanche, P., Degeai, J.-P., Raji, O., Martinez, P., Marcos, C., Von Grafenstein, U., 2016. Extreme storms during the last 6500 years from lagoonal sedimentary archives in the Mar Menor (SE Spain). Climate of the Past 12, 1389–1400. https://doi.org/10.5194/cp-12-1389-2016
Dezileau, L., Sabatier, P., Blanchemanche, P., Joly, B., Swingedouw, D., Cassou, C., Castaings, J., Martinez, P., Von Grafenstein, U., 2011. Intense storm activity during the Little Ice Age on the French Mediterranean coast. Palaeogeography, Palaeoclimatology, Palaeoecology 299, 289–297. https://doi.org/10.1016/j.palaeo.2010.11.009
Farge, M., 1992. Wavelet transforms and their applications to turbulence. Annual review of fluid mechanics 24, 395–458.
Fletcher, W.J., Debret, M., Goñi, M.F.S., 2013. Mid-Holocene emergence of a low-frequency millennial oscillation in western Mediterranean climate: Implications for past dynamics of the North Atlantic atmospheric westerlies. The Holocene 23, 153–166.
Foster, G., 1996. Wavelets for period analysis of unevenly sampled time series. The Astronomical Journal 112, 1709.
Fraedrich, K., 1994. An ENSO impact on Europe? Tellus A 46, 541–552.
Fraedrich, K., 1990. European grosswetter during the warm and cold extremes of the El Niñco/Southern Oscillation. International Journal of Climatology 10, 21–31.
Fraedrich, K., Müller, K., 1992. Climate anomalies in Europe associated with ENSO extremes. International Journal of Climatology 12, 25–31.

Franke, J.G., Werner, J.P., Donner, R.V., 2017. Reconstructing Late Holocene North Atlantic atmospheric circulation changes using functional paleoclimate networks. Climate of the Past 13, 1593–1608. https://doi.org/10.5194/cp-13-1593-2017

Frigola, J., Moreno, A., Cacho, I., Canals, M., Sierro, F.J., Flores, J.A., Grimalt, J.O., Hodell, D.A., Curtis, J.H., 2007. Holocene climate variability in the western Mediterranean region from a deepwater sediment record: HOLOCENE CLIMATE VARIABILITY. Paleoceanography 22. https://doi.org/10.1029/2006PA001307

Gagosian, R.B., Peltzer, E.T., 1986. The importance of atmospheric input of terrestrial organic material to deep sea sediments. Organic Geochemistry 10, 661–669.

Ghaderpour, E., Ince, E.S., Pagiatakis, S.D., 2018. Least-squares cross-wavelet analysis and its applications in geophysical time series. Journal of Geodesy 92, 1223–1236.

Ghaderpour, E., Pagiatakis, S.D., 2019. LSWAVE: a MATLAB software for the least-squares wavelet and cross-wavelet analyses. GPS Solutions 23, 50.

Giraudi, C., 2005. Middle to Late Holocene glacial variations, periglacial processes and alluvial sedimentation on the higher Apennine massifs (Italy). Quaternary Research 64, 176–184.

Giraudi, C., Magny, M., Zanchetta, G., Drysdale, R.N., 2011. The Holocene climatic evolution of Mediterranean Italy: A review of the continental geological data. The Holocene 21, 105–115.

Gouirand, I., Moron, V., 2003. Variability of the impact of El Niño–southern oscillation on sea-level pressure anomalies over the North Atlantic in January to March (1874–1996). International journal of climatology 23, 1549–1566.

GROUP, M., 1970. Observation of formation of deep water in the Mediterranean Sea, 1969.

Harvey, B.J., Shaffrey, L.C., Woollings, T.J., 2015. Deconstructing the climate change response of the Northern Hemisphere wintertime storm tracks. Climate dynamics 45, 2847–2860.

Hasselmann, K., 1976. Stochastic climate models part I. Theory. tellus 28, 473–485.

Held, I.M., Ting, M., Wang, H., 2002. Northern winter stationary waves: Theory and modeling. Journal of climate 15, 2125–2144.

Hochman, A., Saaroni, H., Abramovich, F., Alpert, P., 2019. Artificial Detection of Lower-Frequency Periodicity in Climatic Studies by Wavelet Analysis Demonstrated on Synthetic Time Series. Journal of Applied Meteorology and Climatology 58, 2077–2086.

Honda, M., Nakamura, H., Ukita, J., Kousaka, I., Takeuchi, K., 2001. Interannual seesaw between the Aleutian and Icelandic lows. Part I: Seasonal dependence and life cycle. Journal of climate 14, 1029–1042.

Hurrell, J.W., Kushnir, Y., Ottersen, G., Visbeck, M., 2003. An overview of the North Atlantic oscillation. The North Atlantic Oscillation: climatic significance and environmental impact 134, 1–35.

Jalali, B., Sicre, M.-A., Bassetti, M.-A., Kallel, N., 2016. Holocene climate variability in the north-western Mediterranean Sea (gulf of lions). Climate of the Past Discussions 91–120.

Jalali, B., Sicre, M.-A., Kallel, N., Azuara, J., Combourieu-Nebout, N., Bassetti, M.-A., Klein, V., 2017. High-resolution Holocene climate and hydrological variability from two major Mediterranean deltas (Nile and Rhone). The Holocene 0959683616683258.

Jalut, G., Dedoubat, J.J., Fontugne, M., Otto, T., 2009. Holocene circum-Mediterranean vegetation changes: Climate forcing and human impact. Quaternary International 200, 4–18. https://doi.org/10.1016/j.quaint.2008.03.012

Jaouadi, S., Lebreton, V., Bout-Roumazeilles, V., Siani, G., Lakhdar, R., Boussoffara, R., Dezileau, L., Kallel, N., Mannai-Tayech, B., Combourieu-Nebout, N., 2016. Environmental changes, climate and anthropogenic impact in south-east Tunisia during the last 8 kyr. Climate of the Past 12, 1339–1359. https://doi.org/10.5194/cp-12-1339-2016

Jiménez-Moreno, G., Rodríguez-Ramírez, A., Pérez-Asensio, J.N., Carrión, J.S., López-Sáez, J.A., Villarías-Robles, J.J., Celestino-Pérez, S., Cerrillo-Cuenca, E., León, Á., Contreras,

C., 2015. Impact of late-Holocene aridification trend, climate variability and geodynamic control on the environment from a coastal area in SW Spain. The Holocene 25, 607–617.
Joly, B., Girardot, N., Roulet, B., Labadie, C., 2012. Experimental Daily Forecasts of Northern Atlantic Weather Regimes and Heavy Precipitating Events (HPEs) over Southern France with the Meteo France Global Ensemble System PEARP.
Kelly, B.C., Bechtold, J., Siemiginowska, A., 2009. Are the variations in quasar optical flux driven by thermal fluctuations? The Astrophysical Journal 698, 895.
Kelly, B.C., Becker, A.C., Sobolewska, M., Siemiginowska, A., Uttley, P., 2014. Flexible and scalable methods for quantifying stochastic variability in the ear of massive time-domain astronomical data. ApJ 788, 33. https://doi.org/10.1088/0004-637X/788/1/33
Lebeaupin Brossier, C., Drobinski, P., 2009. Numerical high-resolution air-sea coupling over the Gulf of Lions during two tramontane/mistral events. Journal of Geophysical Research: Atmospheres 114.
Lenoir, G., Crucifix, M., 2018a. A general theory on frequency and time–frequency analysis of irregularly sampled time series based on projection methods–Part 1: Frequency analysis. Nonlinear Processes in Geophysics 25, 145.
Lenoir, G., Crucifix, M., 2018b. A general theory on frequency and time–frequency analysis of irregularly sampled time series based on projection methods–Part 2: Extension to time–frequency analysis. Nonlinear Processes in Geophysics 25.
Lionello, P., Trigo, I.F., Gil, V., Liberato, M.L.R., Nissen, K.M., Pinto, J.G., Raible, C.C., Reale, M., Tanzarella, A., Trigo, R.M., Ulbrich, S., Ulbrich, U., 2016. Objective climatology of cyclones in the Mediterranean region: a consensus view among methods with different system identification and tracking criteria. Tellus A: Dynamic Meteorology and Oceanography 68, 29391. https://doi.org/10.3402/tellusa.v68.29391
Lomb, N.R., 1976. Least-squares frequency analysis of unequally spaced data. Astrophysics and space science 39, 447–462.
Loon, H., Madden, R.A., 1981. The Southern Oscillation. Part I: Global associations with pressure and temperature in northern winter. Monthly Weather Review 109, 1150–1162.
Ludwig, W., Dumont, E., Meybeck, M., Heussner, S., 2009. River discharges of water and nutrients to the Mediterranean and Black Sea: major drivers for ecosystem changes during past and future decades? Progress in Oceanography 80, 199–217.
Magny, M., Bégeot, C., Guiot, J., Peyron, O., 2003. Contrasting patterns of hydrological changes in Europe in response to Holocene climate cooling phases. Quaternary Science Reviews 22, 1589–1596. https://doi.org/10.1016/S0277-3791(03)00131-8
Magny, M., Combourieu-Nebout, N., De Beaulieu, J.L., Bout-Roumazeilles, V., Colombaroli, D., Desprat, S., Francke, A., Joannin, S., Peyron, O., Revel, M., 2013. North-south palaeohydrological contrasts in the central Mediterranean during the Holocene: tentative synthesis and working hypotheses. Climate of the Past Discussions 9, 1901–1967.
Magny, M., de Beaulieu, J.-L., Drescher-Schneider, R., Vannière, B., Walter-Simonnet, A.-V., Miras, Y., Millet, L., Bossuet, G., Peyron, O., Brugiapaglia, E., Leroux, A., 2007. Holocene climate changes in the central Mediterranean as recorded by lake-level fluctuations at Lake Accesa (Tuscany, Italy). Quaternary Science Reviews 26, 1736–1758. https://doi.org/10.1016/j.quascirev.2007.04.014
Magny, M., Miramont, C., Sivan, O., 2002. Assessment of the impact of climate and anthropogenic factors on Holocene Mediterranean vegetation in Europe on the basis of palaeohydrological records. Palaeogeography, Palaeoclimatology, Palaeoecology 186, 47–59.
Magny, M., Peyron, O., Sadori, L., Ortu, E., Zanchetta, G., Vannière, B., Tinner, W., 2012. Contrasting patterns of precipitation seasonality during the Holocene in the south- and

north-central Mediterranean. Journal of Quaternary Science 27, 290–296. https://doi.org/10.1002/jqs.1543

Mann, M.E., Bradley, R.S., Hughes, M.K., 2000. Long-term variability in the El Nino Southern Oscillation and associated teleconnections. Cambridge University Press, Cambridge, UK.

Manzini, E., Giorgetta, M.A., Esch, M., Kornblueh, L., Roeckner, E., 2006. The influence of sea surface temperatures on the northern winter stratosphere: Ensemble simulations with the MAECHAM5 model. Journal of climate 19, 3863–3881.

Maraun, D., Kurths, J., 2004. Cross wavelet analysis: significance testing and pitfalls.

Mariotti, A., Ballabrera-Poy, J., Zeng, N., 2005. Tropical influence on Euro-Asian autumn rainfall variability. Climate Dynamics 24, 511–521.

Mariotti, A., Zeng, N., Lau, K.-M., 2002. Euro-Mediterranean rainfall and ENSO—a seasonally varying relationship. Geophysical research letters 29.

Martin-Puertas, C., Matthes, K., Brauer, A., Muscheler, R., Hansen, F., Petrick, C., Aldahan, A., Possnert, G., van Geel, B., 2012. Regional atmospheric circulation shifts induced by a grand solar minimum. Nature Geoscience 5, 397–401. https://doi.org/10.1038/ngeo1460

Martin-Vide, J., Lopez-Bustins, J.-A., 2006. The western Mediterranean oscillation and rainfall in the Iberian Peninsula. International Journal of Climatology 26, 1455–1475.

Mary, Y., Eynaud, F., Colin, C., Rossignol, L., Brocheray, S., Mojtahid, M., Garcia, J., Peral, M., Howa, H., Zaragosi, S., Cremer, M., 2017. Changes in Holocene meridional circulation and poleward Atlantic flow: the Bay of Biscay as a nodal point. Climate of the Past 13, 201–216. https://doi.org/10.5194/cp-13-201-2017

Mathias, A., Grond, F., Guardans, R., Seese, D., Canela, M., Diebner, H.H., Baiocchi, G., 2004. Algorithms for spectral analysis of irregularly sampled time series. Journal of Statistical Software 11, 1–30.

May, W., Bengtsson, L., 1998. The signature of ENSO in the Northern Hemisphere midlatitude seasonal mean flow and high-frequency intraseasonal variability. Meteorology and Atmospheric Physics 69, 81–100.

Mayewski, P.A., Rohling, E.E., Curt Stager, J., Karlén, W., Maasch, K.A., Meeker, L.D., Meyerson, E.A., Gasse, F., van Kreveld, S., Holmgren, K., Lee-Thorp, J., Rosqvist, G., Rack, F., Staubwasser, M., Schneider, R.R., Steig, E.J., 2004. Holocene Climate Variability. Quaternary Research 62, 243–255. https://doi.org/10.1016/j.yqres.2004.07.001

Moron, V., Gouirand, I., 2003. Seasonal modulation of the El Niño–Southern Oscillation relationship with sea level pressure anomalies over the North Atlantic in October–March 1873–1996. International Journal of Climatology 23, 143–155.

Moy, C.M., Seltzer, G.O., Rodbell, D.T., Anderson, D.M., 2002. Variability of El Niño/Southern Oscillation activity at millennial timescales during the Holocene epoch. Nature 420, 162–165.

Mudelsee, M., Scholz, D., Röthlisberger, R., Fleitmann, D., Mangini, A., Wolff, E.W., 2009. Climate spectrum estimation in the presence of timescale errors. Nonlinear Processes in Geophysics 16, 43–56.

Muñoz-Díaz, D., Rodrigo, F.S., 2005. Influence of the El Niño-Southern Oscillation on the probability of dry and wet seasons in Spain. Climate Research 30, 1–12.

Najac, J., Boé, J., Terray, L., 2009. A multi-model ensemble approach for assessment of climate change impact on surface winds in France. Climate Dynamics 32, 615–634. https://doi.org/10.1007/s00382-008-0440-4

Nigam, S., DeWeaver, E., 2003. Stationary waves (orographic and thermally forced).

Nissen, K.M., Leckebusch, G.C., Pinto, J.G., Renggli, D., Ulbrich, S., Ulbrich, U., 2010. Cyclones causing wind storms in the Mediterranean: characteristics, trends and links to large-scale patterns. Natural Hazards and Earth System Science 10, 1379–1391.

Nuissier, O., Joly, B., Joly, A., Ducrocq, V., Arbogast, P., 2011. A statistical downscaling to identify the large-scale circulation patterns associated with heavy precipitation events over southern France. Quarterly Journal of the Royal Meteorological Society 137, 1812–1827. https://doi.org/10.1002/qj.866

Ólafsdóttir, K.B., Schulz, M., Mudelsee, M., 2016. REDFIT-X: Cross-spectral analysis of unevenly spaced paleoclimate time series. Computers & Geosciences 91, 11–18.

Oppenheim, A.V., 1999. Discrete-time signal processing. Pearson Education India.

Orme, L.C., Reinhardt, L., Jones, R.T., Charman, D.J., Barkwith, A., Ellis, M.A., 2016. Aeolian sediment reconstructions from the Scottish Outer Hebrides: Late Holocene storminess and the role of the North Atlantic Oscillation. Quaternary Science Reviews 132, 15–25.

Ortega, P., Lehner, F., Swingedouw, D., Masson-Delmotte, V., Raible, C.C., Casado, M., Yiou, P., 2015. A model-tested North Atlantic Oscillation reconstruction for the past millennium. Nature 523, 71–74.

Pardo-Igúzquiza, E., Rodríguez-Tovar, F.J., 2012. Spectral and cross-spectral analysis of uneven time series with the smoothed Lomb–Scargle periodogram and Monte Carlo evaluation of statistical significance. Computers & geosciences 49, 207–216.

Peyron, O., Magny, M., Goring, S., Joannin, S., de Beaulieu, J.-L., Brugiapaglia, E., Sadori, L., Garfi, G., Kouli, K., Ioakim, C., Combourieu-Nebout, N., 2013. Contrasting patterns of climatic changes during the Holocene across the Italian Peninsula reconstructed from pollen data. Climate of the Past 9, 1233–1252. https://doi.org/10.5194/cp-9-1233-2013

Plaut, G., Simonnet, E., 2001. Large-scale circulation classification, weather regimes, and local climate over France, the Alps and Western Europe. Climate Research 17, 303–324.

Polanco-Martínez, J.M., Faria, S.H., 2018. Estimation of the significance of the Foster's wavelet spectrum by means of the permutation test, and applications to paleoclimate records.

Pozo-Vázquez, D., Gámiz-Fortis, S.R., Tovar-Pescador, J., Esteban-Parra, M.J., Castro-Díez, Y., 2005. El Niño–Southern Oscillation events and associated European winter precipitation anomalies. International Journal of Climatology 25, 17–31.

Raible, C.C., Luksch, U., Fraedrich, K., 2004. Precipitation and northern hemisphere regimes. Atmospheric Science Letters 5, 43–55.

Raible, C.C., Luksch, U., Fraedrich, K., Voss, R., 2001. North Atlantic decadal regimes in a coupled GCM simulation. Climate Dynamics 18, 321–330.

Raible, C.C., Yoshimori, M., Stocker, T.F., Casty, C., 2007. Extreme midlatitude cyclones and their implications for precipitation and wind speed extremes in simulations of the Maunder Minimum versus present day conditions. Climate Dynamics 28, 409–423. https://doi.org/10.1007/s00382-006-0188-7

Raji, O., Dezileau, L., Von Grafenstein, U., Niazi, S., Snoussi, M., Martinez, P., 2015. Extreme sea events during the last millennium in the northeast of Morocco. Natural Hazards and Earth System Sciences 15, 203.

Rameau, J.-C., Mansion, D., Dumé, G., 1989. Flore forestière française: région méditerranéenne. Forêt privée française.

Randel, W.J., Wu, F., Oltmans, S.J., Rosenlof, K., Nedoluha, G.E., 2004. Interannual changes of stratospheric water vapor and correlations with tropical tropopause temperatures. Journal of the Atmospheric Sciences 61, 2133–2148.

Raynal, O., Bouchette, F., Certain, R., Séranne, M., Dezileau, L., Sabatier, P., Lofi, J., Hy, A.B.X., Briqueu, L., Pezard, P., Tessier, B., 2009. Control of alongshore-oriented sand spits on the dynamics of a wave-dominated coastal system (Holocene deposits, northern Gulf of Lions, France). Marine Geology 264, 242–257. https://doi.org/10.1016/j.margeo.2009.06.008

Reimer, P.J., Bard, E., Bayliss, A., Beck, J.W., Blackwell, P.G., Ramsey, C.B., Buck, C.E., Cheng, H., Edwards, R.L., Friedrich, M., 2013. IntCal13 and Marine13 radiocarbon age calibration curves 0–50,000 years cal BP. Radiocarbon 55, 1869–1887.

Rhein, M., 1995. Deep water formation in the western Mediterranean. Journal of Geophysical Research: Oceans 100, 6943–6959.

Rhines, A., Huybers, P., 2011. Estimation of spectral power laws in time uncertain series of data with application to the Greenland Ice Sheet Project 2 δ18O record. Journal of Geophysical Research: Atmospheres 116.

Rimbu, N., Lohmann, G., Felis, T., Pätzold, J., 2003. Shift in ENSO teleconnections recorded by a northern Red Sea coral. Journal of Climate 16, 1414–1422.

Roberts, N., Brayshaw, D., Kuzucuoğlu, C., Perez, R., Sadori, L., 2011. The mid-Holocene climatic transition in the Mediterranean: Causes and consequences. The Holocene 21, 3–13. https://doi.org/10.1177/0959683610388058

Roberts, N., Moreno, A., Valero-Garcés, B.L., Corella, J.P., Jones, M., Allcock, S., Woodbridge, J., Morellón, M., Luterbacher, J., Xoplaki, E., 2012. Palaeolimnological evidence for an east–west climate see-saw in the Mediterranean since AD 900. Global and Planetary Change 84, 23–34.

Rogers, J.C., 1997. North Atlantic storm track variability and its association to the North Atlantic Oscillation and climate variability of northern Europe. Journal of Climate 10, 1635–1647.

Sabatier, P., Bruno, W., Francesco, F.G., Fanny, M., Jérôme, P., Anne-Lise, D., Adeline, B., Wentao, C., Cécile, P., Jean-Louis, R., Ludovic, G., Manon, B., Yves, P., Emmanuel, M., Pierre, T., Fabien, A., 2017. 6-kyr record of flood frequency and intensity in the western Mediterranean Alps – Interplay of solar and temperature forcing. Quaternary Science Reviews 170, 121–135. https://doi.org/10.1016/j.quascirev.2017.06.019

Sabatier, P., Dezileau, L., 2010. Archives sédimentaires dans les lagunes du Golfe d'Aigues-Mortes. Estimation de l'aléa de tempête depuis 2000 ans. Quaternaire. Revue de l'Association française pour l'étude du Quaternaire 21, 5–11.

Sabatier, P., Dezileau, L., Briqueu, L., Colin, C., Siani, G., 2010. Clay minerals and geochemistry record from northwest Mediterranean coastal lagoon sequence: Implications for paleostorm reconstruction. Sedimentary Geology 228, 205–217. https://doi.org/10.1016/j.sedgeo.2010.04.012

Sabatier, P., Dezileau, L., Colin, C., Briqueu, L., Bouchette, F., Martinez, P., Siani, G., Raynal, O., Von Grafenstein, U., 2012. 7000 years of paleostorm activity in the NW Mediterranean Sea in response to Holocene climate events. Quaternary Research 77, 1–11. https://doi.org/10.1016/j.yqres.2011.09.002

Sabatier, P., Dezileau, L., Condomines, M., Briqueu, L., Colin, C., Bouchette, F., Le Duff, M., Blanchemanche, P., 2008. Reconstruction of paleostorm events in a coastal lagoon (Hérault, South of France). Marine Geology 251, 224–232. https://doi.org/10.1016/j.margeo.2008.03.001

Sabatier, P., Nicolle, M., Piot, C., Christophe, C., Debret, M., Swingedouw, D., Perrette, Y., Bellingery, M.-C., Chazeau, B., Develle, A.-L., 2020. Past African dust inputs in the western Mediterranean area controlled by the complex interaction between the Intertropical Convergence Zone, the North Atlantic Oscillation, and total solar irradiance. Climate of the Past 16, 283–298.

Sadori, L., Giardini, M., Gliozzi, E., Mazzini, I., Sulpizio, R., van Welden, A., Zanchetta, G., 2015. Vegetation, climate and environmental history of the last 4500 years at lake Shkodra (Albania/Montenegro). The Holocene 25, 435–444.

Scargle, J.D., 1982. Studies in astronomical time series analysis. II-Statistical aspects of spectral analysis of unevenly spaced data. The Astrophysical Journal 263, 835–853.

Schroeder, K., Josey, S.A., Herrmann, M., Grignon, L., Gasparini, G.P., Bryden, H.L., 2010. Abrupt warming and salting of the Western Mediterranean Deep Water after 2005: atmospheric forcings and lateral advection. Journal of Geophysical Research: Oceans 115.

Schulz, M., Mudelsee, M., 2002. REDFIT: estimating red-noise spectra directly from unevenly spaced paleoclimatic time series. Computers & Geosciences 28, 421–426.

Schulz, M., Stattegger, K., 1997. SPECTRUM: Spectral analysis of unevenly spaced paleoclimatic time series. Computers & Geosciences 23, 929–945.

Sgubin, G., Swingedouw, D., Drijfhout, S., Mary, Y., Bennabi, A., 2017. Abrupt cooling over the North Atlantic in modern climate models. Nature Communications 8.

Siani, G., Magny, M., Paterne, M., Debret, M., Fontugne, M., 2013. Paleohydrology reconstruction and Holocene climate variability in the South Adriatic Sea. Climate of the Past 9, 499–515. https://doi.org/10.5194/cp-9-499-2013

Sicre, M.-A., Jalali, B., Martrat, B., Schmidt, S., Bassetti, M.-A., Kallel, N., 2016. Sea surface temperature variability in the North Western Mediterranean Sea (Gulf of Lion) during the Common Era. Earth and Planetary Science Letters 456, 124–133. https://doi.org/10.1016/j.epsl.2016.09.032

Smith, A.C., Wynn, P.M., Barker, P.A., Leng, M.J., Noble, S.R., Tych, W., 2016. North Atlantic forcing of moisture delivery to Europe throughout the Holocene. Scientific Reports 6. https://doi.org/10.1038/srep24745

Solanki, S.K., Usoskin, I.G., Kromer, B., Schüssler, M., Beer, J., 2004. Unusual activity of the Sun during recent decades compared to the previous 11,000 years. Nature 431, 1084–1087.

Sorrel, P., Debret, M., Billeaud, I., Jaccard, S.L., McManus, J.F., Tessier, B., 2012. Persistent non-solar forcing of Holocene storm dynamics in coastal sedimentary archives. Nature Geoscience 5, 892–896. https://doi.org/10.1038/ngeo1619

Sorrel, P., Tessier, B., Demory, F., Delsinne, N., Mouazé, D., 2009. Evidence for millennial-scale climatic events in the sedimentary infilling of a macrotidal estuarine system, the Seine estuary (NW France). Quaternary Science Reviews 28, 499–516.

Steinhilber, F., Abreu, J.A., Beer, J., Brunner, I., Christl, M., Fischer, H., Heikkilä, U., Kubik, P.W., Mann, M., McCracken, K.G., 2012. 9,400 years of cosmic radiation and solar activity from ice cores and tree rings. Proceedings of the National Academy of Sciences 109, 5967–5971.

Stocker, T.F., Qin, D., Plattner, G.K., Tignor, M., Allen, S.K., Boschung, J., Nauels, A., Xia, Y., Bex, V., Midgley, P.M., 2013. IPCC, 2013: summary for policymakers in climate change 2013: the physical science basis, contribution of working group I to the fifth assessment report of the intergovernmental panel on climate change. Cambridge University Press, Cambridge, New York, USA.

Stuiver, M., Braziunas, T.F., 1989. Atmospheric 14C and century-scale solar oscillations. Nature 338, 405–408.

Toreti, A., Xoplaki, E., Maraun, D., Kuglitsch, F.-G., Wanner, H., Luterbacher, J., 2010. Characterisation of extreme winter precipitation in Mediterranean coastal sites and associated anomalous atmospheric circulation patterns. Natural Hazards and Earth System Sciences 10, 1037–1050.

Torrence, C., Compo, G.P., 1998. A practical guide to wavelet analysis. Bulletin of the American Meteorological society 79, 61–78.

Torrence, C., Webster, P.J., 1999. Interdecadal changes in the ENSO–monsoon system. Journal of climate 12, 2679–2690.

Trigo, I.F., Davies, T.D., Bigg, G.R., 1999. Objective climatology of cyclones in the Mediterranean region. Journal of Climate 12, 1685–1696.

Trigo, R.M., DaCamara, C., 2000. Circulation weather types and their influence on the precipitation regime in Portugal. International Journal of Climatology 20, 1559–1581.

Tsonis, A.A., 2009. Dynamical changes in the ENSO system in the last 11,000 years. Climate dynamics 33, 1069.
Ulses, C., Estournel, C., Puig, P., Durrieu de Madron, X., Marsaleix, P., 2008. Dense shelf water cascading in the northwestern Mediterranean during the cold winter 2005: Quantification of the export through the Gulf of Lion and the Catalan margin. Geophysical Research Letters 35.
Usoskin, I.G., Gallet, Y., Lopes, F., Kovaltsov, G.A., Hulot, G., 2016. Solar activity during the Holocene: the Hallstatt cycle and its consequence for grand minima and maxima. Astronomy & Astrophysics 587, A150.
Vanniere, B., Galop, D., Rendu, C., Davasse, B., 2001. Feu et pratiques agro-pastorales dans les Pyrénées-Orientales: le cas de la montagne d'Enveitg (Cerdagne, Pyrénées-Orientales, France). Sud-Ouest Européen 11, 29–42.
Walker, M.J., Berkelhammer, M., Björck, S., Cwynar, L.C., Fisher, D.A., Long, A.J., Lowe, J.J., Newnham, R.M., Rasmussen, S.O., Weiss, H., 2012. Formal subdivision of the Holocene Series/Epoch: a Discussion Paper by a Working Group of INTIMATE (Integration of ice-core, marine and terrestrial records) and the Subcommission on Quaternary Stratigraphy (International Commission on Stratigraphy). Journal of Quaternary Science 27, 649–659.
Welch, P., 1967. The use of fast Fourier transform for the estimation of power spectra: a method based on time averaging over short, modified periodograms. IEEE Transactions on audio and electroacoustics 15, 70–73.
Winschall, A., Sodemann, H., Pfahl, S., Wernli, H., 2014. How important is intensified evaporation for Mediterranean precipitation extremes? Journal of Geophysical Research: Atmospheres 119, 5240–5256. https://doi.org/10.1002/2013JD021175
Wirth, S.B., Glur, L., Gilli, A., Anselmetti, F.S., 2013. Holocene flood frequency across the Central Alps–solar forcing and evidence for variations in North Atlantic atmospheric circulation. Quaternary Science Reviews 80, 112–128.
Witt, A., Schumann, A.Y., 2005. Holocene climate variability on millennial scales recorded in Greenland ice cores.
Woollings, T., Gregory, J.M., Pinto, J.G., Reyers, M., Brayshaw, D.J., 2012. Response of the North Atlantic storm track to climate change shaped by ocean–atmosphere coupling. Nature Geoscience 5, 313–317. https://doi.org/10.1038/ngeo1438
Xoplaki, E., 2002. Climate variability over the Mediterranean. PhD, University of Bern, Switzerland.
Zazo, C., Dabrio, C.J., Goy, J.L., Lario, J., Cabero, A., Silva, P.G., Bardají, T., Mercier, N., Borja, F., Roquero, E., 2008. The coastal archives of the last 15 ka in the Atlantic–Mediterranean Spanish linkage area: Sea level and climate changes. Quaternary International 181, 72–87.
Zhang, Z., Moore, J., 2011. Intrinsic feature extraction in the COI of wavelet power spectra of climatic signals, in: 2011 4th International Congress on Image and Signal Processing. IEEE, pp. 2354–2356.
Zielhofer, C., Fletcher, W.J., Mischke, S., De Batist, M., Campbell, J.F., Joannin, S., Tjallingii, R., El Hamouti, N., Junginger, A., Stele, A., 2017. Atlantic forcing of Western Mediterranean winter rain minima during the last 12,000 years. Quaternary Science Reviews 157, 29–51.